REPORT DOCUMENTATION PAGE

Form Approved
OMB NO. 0704-0188

1. AGENCY USE ONLY (Leave Blank)	2. REPORT DATE November 1999	3. REPORT TYPE AND DATES COVERED Final Report

4. TITLE AND SUBTITLE
Titanium Carbosulfides and the Fracture Toughness of Ultra High Strength Steels

5. FUNDING NUMBERS
DAAH04-93-G-0083

6. AUTHOR(S)
Warren M. Garrison Jr.

7. PERFORMING ORGANIZATION NAME(S) AND ADDRESS(ES)
Carnegie-Mellon University
Pittsburgh, PA 15213

8. PERFORMING ORGANIZATION REPORT NUMBER

9. SPONSORING / MONITORING AGENCY NAME(S) AND ADDRESS(ES)
U. S. Army Research Office
P.O. Box 12211
Research Triangle Park, NC 27709-2211

10. SPONSORING / MONITORING AGENCY REPORT NUMBER
ARO 30912.1-MS

11. SUPPLEMENTARY NOTES
The views, opinions and/or findings contained in this report are those of the author(s) and should not be construed as an official Department of the Army position, policy or decision, unless so designated by other documentation.

12 a. DISTRIBUTION / AVAILABILITY STATEMENT
Approved for public release; distribution unlimited.

12 b. DISTRIBUTION CODE

13. ABSTRACT (Maximum 200 words)

The objectives of this work were to calculate from first principles the work of adhesion associated with the steel-MnS and steel-Ti_2CS interfaces and to examine with transmission electron microscopy void nucleation at particles of MnS and particles of Ti_2CS in steel. The motivation for this work was the observation that gettering sulfur as Ti_2CS rather than as MnS leads to doubling and even tripling of the fracture toughness of some ultra-high strength steels and that these improvements in toughness were believed to be due to particles of Ti_2CS being much more

continued on next page

14. SUBJECT TERMS			15. NUMBER OF PAGES 16. PRICE CODE
17. SECURITY CLASSIFICATION OR REPORT UNCLASSIFIED	18. SECURITY CLASSIFICATION ON THIS PAGE UNCLASSIFIED	19. SECURITY CLASSIFICATION OF ABSTRACT UNCLASSIFIED	20. LIMITATION OF ABSTRACT UL

NSN 7540-01-280-5500

Standard Form 298 (Rev.2-89)
Prescribed by ANSI Std. 239-18
298-102

resistant to void nucleation than particles of MnS. The results are as follows. Using the LKKR approach the bulk properties and surface energies of MnS and F.C.C. iron were calculated as was the interface energy of a MnS-steel interface. With these the results the work of adhesion for this interface was determined. The bulk properties of Ti_2CS were determined but we were unable to obtain reasonable results for a Ti_2CS-steel interface. The investigations of void nucleation at particles of MnS and Ti_2CS in two different heats of an austenitic 0.07/30Ni steel were surprising. In this material it was found that voids were first nucleated at both inclusion types at strains as low as 0.20. It had been expected that voids would be first nucleated at the particles of MnS at these low strains but that voids would not be observed at the particles of Ti_2CS until the strains had exceeded at least one.

Titanium Carbosulfides and the Fracture Toughness of Ultra High Strength Steels

Warren M. Garrison Jr.
Department of Materials Science and Engineering
Carnegie Mellon University

Final Technical Report to the
Army Research Office
ARO Grant Number: DAAH04-93-0083

ARO Proposal Number: 30192-MS

Period of 4/1/93 - 9/30/96

Attention: Dr. Wilbur C. Simmons or Dr. David Stepp

Materials Science Division
Army Research Office
Post Office Box 12211
Research Triangle Park, NC 27709

or

Material Science Division
U.S. Army Research Office
4300 S. Miami Blvd.
Durham, NC 27703

Table of Contents

List of Figures

List of Tables

1. Background

Ductile fracture in ultra-high strength steels—steels that have strength levels exceeding 1200 MPa and used for critical applications such as aircraft and automobile components—proceeds by the growth and coalescence of voids nucleated at inclusions (like oxides and/or sulfides) or other second phase particles. The microstructure of these steels can be considered as having *primary particles* distributed in a *fine-scale microstructure*. The primary particles are those which nucleate voids first, and are typically either oxides or sulfides. The rest of the microstructure, including possibly some *other* particles such as carbides, comprises the fine scale microstructure. It is believed that the fine-scale microstructure has an inherent toughness that is decreased by the presence of the primary particles. Therefore, minimizing the detrimental effects of inclusions (which act as primary particles) on the fracture toughness is an important goal in the design of high strength, high toughness steels.

It has been shown (Handerhan et al., 1989; Maloney and Garrison, 1989) that an effective way of minimizing the detrimental effects of inclusions in ultra-high strength steels has been to getter sulfur as particles of titanium carbosulfide(Ti_2CS) rather than as particles of manganese or chromium sulfide (MnS, CrS) or lanthanum oxysulfide(La_2O_2S). Gettering the sulfur as Ti_2CS instead of as MnS or La_2O_2S results in vast improvements in toughness, though the extent of improvement depends on the fine-scale microstructure. The same authors further suggested that their observations are a consequence of the carbosulfide particles being more resistant to void nucleation than particles of MnS, CrS or La_2O_2S. However, the differences in the void nucleation resistance of the different particle types are not understood. Since this early work, the carbosulfide effect has been shown to be present in steels with moderate strength levels (such as a 9-Ni steel with strength ~ 900 MPa) also, suggesting that the effect could be fairly general and therefore with the potential to be beneficially applied to other systems, especially if the effect could be understood and manipulated. Accordingly, the main goal of the current work is to improve understanding of the void nucleation behavior at two different particle types, namely MnS and Ti_2CS, which are present in a steel matrix.

In spite of an extensive literature (for instance, see the review on ductile fracture by Garrison and Moody(Garrison and Moody, 1987)) on both experimental and theoretical studies devoted to void nucleation, the present understanding of the phenomenon is fairly rudimentary. Void nucleation at second phase particles can occur either by particle fracture or by decohesion of the particle-matrix interface. In either case, the above-mentioned studies indicate that void nucleation

is possibly influenced by several factors – amongst these are the particle size, particle size distribution, inter-particle spacing, particle morphology, the structure and bonding at the particle-matrix interface, the flow stress of the matrix and the relative physical properties of the particle (such as the elastic modulii and the thermal expansion coefficient) with respect to the matrix. The relative importance of the different factors in influencing void nucleation is not known. There is also considerable confusion regarding the effect of the different factors on void nucleation – for instance, consider the effect of particle size(Garrison and Moody, 1987) at constant volume fraction: while some studies predict that it is difficult to nucleate voids at smaller particles, others suggest that void nucleation is more difficult at larger particles. There are also studies which predict that there will be no size dependence at all. Thus, at present, no unified model of void nucleation (that can be used to predict void nucleation behavior in a given system) exists, and the phenomenon continues to be rather poorly understood.

Nevertheless, most of the prior studies suggest an important role played by the particle-matrix interface in determining void nucleation resistance when failure initiation results from decohesion of the particle-matrix interface. That interface decohesion was observed to be the predominant means of void nucleation in the earlier studies on high-strength steels suggests it is important to investigate the structure and energetics of Ti_2CS-matrix and MnS-matrix interfaces in order to better understand the void nucleation at these interfaces.

When void nucleation occurs by decohesion at the particle-matrix interface, it is considered extremely likely that the strength of the interface has a significant role to play in determining the void nucleation resistance. A measure of the strength of an interface is its *work of adhesion* (W_{ad}) which is defined as

$$W_{ad} = \gamma_p + \gamma_m - \gamma_{pm} \qquad (1)$$

where γ_p and γ_m are the surface energies associated with the free particle and matrix surfaces respectively, and γ_{pm} is the excess energy associated with the particle-matrix interface. A higher work of adhesion is thought to result in an enhanced resistance to void nucleation. The work of adhesion is intimately related to the bonding at the interface – differences in the work of adhesion therefore likely reflect the variations in the chemical interactions between the two phases at the atomic level. From (1), it can be seen that two surface energies and one interface energy need to be known to determine the work of adhesion – the experimental determination of these quantities is in general rather difficult and in the systems of interest, almost impossible. Therefore, it was decided to adopt a computational approach in the present work to obtain the work of adhesion at interfaces of MnS and Ti_2CS particles with a steel matrix.

Thus the main objectives of the present work were to investigate, using both experimental and computational techniques, the differences in void nucleation behavior and the strength of the respective interfaces at MnS and Ti_2CS particles in a steel matrix. The main issues and the objectives are detailed in the following section.

2. Issues and objectives

Significant research has been done in earlier studies (Handerhahn, 1987; Maloney, 1992; Wojcieszynski, 1993) to understand the role of second phase particles in determining the fracture toughness of UHS steels. In these studies, the dependence of fracture toughness on various factors such as the particle type, particle spacing, the fine scale microstructure and the grain size of the matrix were investigated. As mentioned earlier, it has been found that an effective way to increase toughness is to getter the sulfur as Ti_2CS and that the improvement comes from an enhanced void nucleation resistance of the Ti_2CS particles. It is important, from a materials design perspective, to investigate the void nucleation behavior of Ti_2CS and MnS particles. Several factors might play a role in the enhanced void nucleation resistance of the Ti_2CS particles – particle morphology, particle orientation with respect to loading direction (in case of non-spherical and non-equiaxed particles), internal bonding within Ti_2CS (which might influence the interfacial bonding), and the structure and the strength (as indicated by the W_{ad} for example) of the MnS/matrix and the Ti_2CS/matrix interfaces. The overall goal of the current work has been to address the differences in void nucleation behavior of the MnS and Ti_2CS particles with reference to the factors mentioned above. The work can be divided into two categories, namely experimental and computational.

The main objective of the experimental work has been to examine void nucleation at particles of MnS and Ti_2CS in steel. An austenitic matrix appeared to offer several advantages (see §3.1.1) over a martensitic matrix and therefore it was decided to perform the experimental investigation using a model austenitic alloy. The experimental work has involved:

(a) designing the base composition of a model system,

(b) making two different heats of this model system, one containing MnS particles and the other containing Ti_2CS particles,

(c) verifying the superior void nucleation resistance of the Ti_2CS particles (as compared to the MnS inclusions) in this system,

(d) performing as thorough a particle characterization as possible to determine the average size, inter-particle spacing, chemistry and orientation relationship with the matrix (if any), and

(e) investigating the early stages of void nucleation using transmission electron microscopy.

The objectives of the computational work have been: (i) to investigate the bonding in bulk Ti_2CS, (ii) to investigate the bonding at MnS/matrix and Ti_2CS/matrix interfaces, and (iii) to compute the work of adhesion for MnS/matrix and Ti_2CS/matrix interfaces. The computational work has involved:

(a) performing calculations for bulk phases of γ-Fe (to simulate the austenitc matrix of the model material), MnS and Ti_2CS both to investigate the properties (such as the equilibrium lattice constants, bulk modulii and total energies) of the bulk solids themselves and also to provide input to subsequent surface and interface calculations

(b) performing calculations on systems containing interfaces of different particle types in γ-Fe to obtain interface energies and to investigate the bonding at the interfaces

(c) performing calculations on semi-bulk systems to obtain surface energies corresponding to those involved in forming the different interfaces mentioned above, and

(d) computing the work of adhesion using the values of interface and surface energies obtained from (b) and (c) above.

The approach used to achieve these objectives is outlined in the following section.

3. Approach and methodology

3.1. Experimental

The approach adopted for the experimental studies was in accord with the objectives stated in §2. Briefly, it was desired to investigate, using both scanning and transmission electron microscopy, the void nucleation behavior at Ti_2CS and MnS particles in a model austenitic steel matrix.

3.1.1. Microstructure, composition and heat treatment

Microstructure – The desired microstructure dictated the composition of the material. Two heats of this material are required, one with MnS particles and the other with Ti_2CS. An austenitic matrix was preferred because of the following reasons: (a) the presence of an austenite↔martensite transformation could lead to the presence of a significant amount of retained austenite in a martensitic microstructure, and a dual phase matrix was not conducive to the proposed study; also, retained austenite could be present at the particle-matrix interfaces and this could significantly alter the strength and void nucleation behavior of these interfaces, (b) the martensitic microstructure, with its lath-like nature and high dislocation density, makes TEM studies of small particles (and their interfaces with the matrix) very difficult; an austenitic matrix, on the other hand, with its relatively featureless microstructure and a lower dislocation density is

ideally suited for such studies, and (c) finally, it would be useful from an applications standpoint to know whether the beneficial effect of Ti_2CS particles is also valid for an austenitic matrix. Thus, the most desired microstructure for the present study would be a featureless austenitic matrix in which were dispersed numerous fine particles of either MnS or Ti_2CS – a low particle density would make the TEM studies impractical (because particles will then not be found on each and every thin foil) and larger particles may either nucleate by particle fracture (not the desired mode) and/or exhibit interfacial characteristics different from those of the fine particles found in the ultra high strength steels.

Composition – In order to achieve a simple microstructure, it was decided to minimize the number of alloying elements. Accordingly, only one major austenite stabilizer, namely Ni, besides carbon was added to keep the matrix austenitic. The nominal composition (weight %) of the material was: 0.08C/38Ni/.006S/balance Fe. The sulfur content was decided so as to achieve an optimum inclusion density. It was decided to add 0.5 weight percent manganese to one heat and 0.02 weight percent titanium to the other heat in order to precipitate particles of MnS and Ti_2CS respectively. The actual compositions of the two heats are given in Table 1.

Heat Treatment – It was desirable to eliminate/reduce the presence of carbides in the microstructure so that the main second phase particles, besides the oxides, would be the inclusions of interest. Specimens from the as-forged material were solutionized at three different temperatures, viz. 1000°C, 1050°C and 1100°C for one hour and oil-quenched. Thin foils were prepared from these specimens and examined in the TEM. The specimens from the two lower solutionizing temperatures showed the presence of carbides while those treated at 1100°C did not – hence all the specimens used to achieve the experimental objectives were subjected to the solutionizing treatment at 1100°C.

3.1.2. Tensile properties

Smooth axisymmetric 0.25" gage diameter tensile specimens (which conformed to the ASTM E8 standard) were used to: (a) characterize the two heats in terms of the mechanical properties such as the true failure strain, yield and ultimate tensile strengths, and the reduction in area, (b) verify indirectly whether the Ti_2CS effect is present in this material by inspecting the true strain to failure (which was higher for the Ti_2CS heat than for the MnS heat in the previous studies), and (c) provide samples for SEM and TEM investigations of void nucleation.

3.1.3. Particle characterization

3.1.3.1. Volume fraction, average particle size and inter-particle spacing

Smooth polished cross-sections of the two heats were examined in the SEM to determine the particle volume fraction, the average particle size and the three-dimensional inter-particle spacing. A metallographic procedure specially devised for this austenitic material was used in the preparation of the samples for SEM examination. In the SEM, images of 25-40 randomly chosen areas of the specimen were taken at magnifications of 3000-5000x; the dimensions of the particles found in these frames were tagged, and their major and minor axes (a and b) measured from which the apparent area ($=\pi ab$) was computed. From the area, an equivalent apparent spherical diameter d was calculated. The harmonic mean of inclusion diameters was calculated from $H(d) = N/\Sigma_i(1/d_i)$ (Ashby and Ebeling, 1966) where N is the total number of particles. The average particle radius R_o was then derived from $R_o = (\pi/4)H(d)$. The three-dimensional nearest neighbor spacing was calculated from $X_o = 0.89R_of^{(-1/3)}$ (Ashby and Ebeling, 1966) where f is the particle volume fraction.

3.1.3.2. Shape and chemistry

Both scanning and transmission microscopy techniques were employed to investigate the shape and chemistry of the particles. All the microscopes used were equipped with a PGT System 4 energy dispersive x-ray spectrometer. The scanning microscope was employed mainly to examine fracture surfaces where it has good resolution even at large working distances that were required to perform an energy-dispersive analysis of the inclusion x-ray spectrum. Smooth polished cross-sectional samples were also examined in the SEM to analyze the chemistry of particles larger than 250nm. It was difficult to infer the shape of the particles from back-scattered electron images unless the particles were quite large.

Both carbon replicas and thin foils were examined in the TEM to characterize particles that were too small to be characterized using the SEM. The replicas were prepared from polished samples as follows: the sample surfaces were cleaned with cellulose acetate replicating tape and were lightly etched with 2% nital to bring the inclusions in relief. Then the sample surface was deposited with a thin layer of carbon. The carbon film was scribed into small pieces (2mm x 2mm) and floated off the sample by immersing the sample in 4% nital solution. The pieces were rinsed in a series of ethanol-water solutions of increasing water concentration and were captured on copper grids and dried before storage.

It was found that a combination of twin jet electro-polishing and ion-milling yielded optimal results for thin foils which were prepared as follows: slices of material 0.020" thick were cut from

specimen blanks using a slow speed saw with rubber-bonded silica grinding wheel. The slices were wax-mounted on a flat metal piece and ground to a thickness of 0.007". 3mm diameter discs were punched out of these slices and then jet-polished in a Fischione twin jet polishing unit using 10% perchloric acid in ethanol solution at –42°C. It was found that an initial setting of 20V gave satisfactory results. Examination of as jet-polished foils in the TEM revealed some artifacts due to the polishing, mainly preferential etching around particles. It was found that a subsequent ion-milling step removed the polishing artifacts and foils with no preferential etching were consistently obtained. The ion-milling was done at room temperature using beam angles ~ 12° at 5kV for an hour. The milling results were substantially improved if the Precision Ion Polishing System (PIPS™ manufactured by Gatan, Inc.) was used instead of conventional ion-milling. The configuration of the PIPS makes it possible to clean the as-jet-polished foil using very low beam angles (~ 5°), low voltage (~ 3 kV) and very short times (10 minutes or less). Thus, thin foil specimen preparation was optimized by combining jet polishing with subsequent ion-milling to produce foils with largely reduced artifacts; in particular, a procedure was established through which preferential etching around particles was completely eliminated.

The thin foil specimens were also used to detect the presence of carbon in inclusions in the Ti_2CS heat. These studies were carried out through parallel electron energy loss spectroscopy (PEELS) and energy filtered imaging using the Gatan Imaging Filter setup in conjunction with a 400kV JEOL 4000EX electron microscope.

3.1.4. Void generation characteristics

3.1.4.1. Void nucleation strain

Axisymmetric tensile specimens, either fractured or strained close to fracture, were employed to obtain the void volume fraction as a function of strain. Each specimen was mechanically ground longitudinally to a level just above (about 0.012") its mid-plane. The strained area close to the neck was cut and mounted in blue diallyl phthalate. The mounted specimen was metallographically polished until the mid-plane was reached. This was ensured by comparing measurements of the specimen width (at the neck and at fixed distances away from the neck) obtained before the sample was ground and after polishing. The measurements were made using an optical measuring microscope with a sensitivity of 0.001mm. The polished specimen was then examined in the scanning electron microscope – regions at different distances from the neck (and hence at different strain levels) were chosen and 8-10 pictures were taken (at a suitable magnification) close to the central axis for every strain level. The void area fraction was measured in a manner similar to the measurement of the inclusion area fraction as outlined in the

previous section. It must be mentioned that as it is difficult to distinguish voids from the inclusions, what was measured was the fraction of voids *and* inclusions. This void+inclusion volume fraction was then divided by the inclusion volume fraction to obtain the normalized void volume fraction at a given strain level. The true strain at a given distance from the neck was found using $\varepsilon = 2 \ln(d_o/d_i)$ where d_o is the original gage diameter of the unstrained specimen and d_i is the diameter of the strained specimen at the point of interest. The diameter measurements were made using the optical measuring microscope mentioned above.

3.1.4.2. TEM studies of void nucleation

Methods of scanning electron microscopy lack the resolution to detect the initial stages of void nucleation, especially when the particle sizes are less than 0.1μ. Owing to this limitation, it was decided to monitor the void nucleation features as a function of strain using thin foil TEM methods. The objectives in this aspect of the work were (i) to determine the strain at which voids are first observed, (ii) to determine whether there are any morphology induced preferred void nucleation sites, and (iii) to determine whether there were obvious size effects with respect to void nucleation. To realize these objectives, it was necessary to make thin foils from strained axisymmetric tensile specimens. The establishment of the foil preparation technique described above (§3.1.3.2) was crucial to this task because had preferential etching at interfaces not been eliminated, it would be have been impossible to distinguish voids from holes created by etching during foil preparation.

Thin foils for this work were prepared as follows: tensile specimens were strained either to fracture or to a strain very close to fracture. Tensile specimens with gage section diameters of either 0.25" or 0.55" were used for this purpose – the larger diameter specimens were necessary because, with the standard 0.25" dia. specimens the regions of high strain ($\varepsilon > 1$) were less than 3mm in diameter and therefore were unsuitable for use in the TEM which requires 3mm diameter disc specimens. However, it was possible to examine the standard specimens at lower strain levels.

In order to be able to locate the position of the voids with respect to the tensile axis, it was decided to examine foils in the longitudinal orientation, i.e. with the tensile axis in the plane of the foil. Two different methods were adopted to obtain thin slices from the strained specimens in this orientation: (i) the specimens were wire-cut using 0.004" or 0.006" wires to produce longitudinal sections 0.010" thick – the slices in the center were then ground to a thickness of 0.007" using 600 grit paper, or (ii) the specimen was mounted in wax and precision ground parallel to the tensile axis to just above the mid-plane, turned over and then ground from the other side to a total thickness of 0.010" – this section was unmounted and ground to 0.007" using 600

grit paper; only one section was obtained in this method as opposed to the first method where multiple slices at different distances from the center were obtained. Subsequent stages of foil preparation were identical irrespective of the method used to obtain the slices. A line was drawn on the slice to mark the tensile axis and 3mm discs were then punched out along this line. After punching, the position of the tensile axis was marked at either end with a sharp knife-edge blade to facilitate identification of the tensile axis. The discs were electropolished and ion-milled using the PIPS in a manner identical to the regular thin foils.

3.2. Computational

3.2.1. General considerations

As stated earlier, the main objective of the computational work is to obtain the work of adhesion at different inclusion-matrix interfaces, and from (1) it can be seen that W_{ad} depends on two surface energies and one interface energy – this implies that the main goal of the computations would be to obtain these values.

For our computations, we have used the Layer Korringa Kohn Rostoker (LKKR) method (MacLaren et al., 1989) which is derived from the original KKR multiple scattering technique. There are many different ab-initio codes that are presently available, but most of these demand full three-dimensional crystal periodicity and are thus unsuitable for a direct application to systems containing surfaces and interfaces. The LKKR method is unique in that it decomposes the 3-D solid into layers and requires periodicity only within each layer (2-D requirement instead of 3-D). This particular feature renders it more suitable to handle surface and interface systems within the same framework as that of bulk systems. In the following subsections, the LKKR method and its application to bulk, surface and interface systems is presented.

3.2.2. The LKKR method

Many ab-initio calculations relevant to metallurgy and materials science have their roots in electron theory. The objective is to solve Schroedinger's equation for the charge densities and energy eigenstates of the system under study. This is a many-electron problem of reasonable complexity to which exact solutions are intractable even for the simplest of systems. An important breakthrough came from Hohenberg, Kohn and Sham in the early sixties. They introduced the concept of Density Functional Theory (DFT) which transforms the many-electron problem into an equivalent single-electron problem that could then be solved within the so-called Local Density Approximation (LDA).

DFT deals with the ground state of an interacting electron gas in an external potential $v(\mathbf{r})$ and is based on the assertion that: (i) the electron density $n(\mathbf{r})$ determines all aspects of the

electronic structure of the system, and (ii) the total energy of the system is a functional of the charge density, i.e., $E = F[n(\mathbf{r})]$ – the triumph of DFT lies in the proof (due to Hohenberg and Kohn) that the energy functional has as its minimum value the correct ground-state energy associated with $v(\mathbf{r})$. Therefore, the ground state energy can be obtained by variationally minimizing the energy with respect to the charge density.

The LKKR method employs a muffin-tin potential, dividing space into spherical and interstitial regions. The 3-D solid is partitioned into layers. Each layer is assumed to possess full translational (Bloch) periodicity and the scattering properties of each layer are calculated using partial wave bases (spherical harmonics) in the spherical regions and plane-wave bases in the interstitial regions. The different layers are coupled using a plane-wave basis to re-create the scattering properties of the entire solid. The ground state charge density is derived by solving the Schroedinger's equation using a Green's function formalism within multiple scattering theory. The complex (in the mathematical sense) one electron Green's function is dependent on position $\mathbf{r}$, the 2-D wave vector $\mathbf{k}$, the energy E and the spin σ. The local energy-resolved density of states, $\rho(r,E,\sigma)$, is related to the one electron Green's function as follows:

$$\rho(\mathbf{r},E,\sigma) = -\frac{1}{\pi}\,\mathrm{Im}\int d\mathbf{k}.G(\mathbf{r},\mathbf{k},E,\sigma) \qquad (2)$$

where the integration is over the 2-D Brillouin zone. The ground state charge density, $n(\mathbf{r})$, is then obtained by further integrating ρ over an appropriate energy range. The density of states (which is a $\rho(E)$ versus E plot) is obtained by integrating $\rho(\mathbf{r},E)$ over an appropriate volume (either the individual atomic volume or the entire unit cell). In a spin-polarized calculation, there will be two different density of states, one for spin-up and another for spin-down electrons. Once $n(\mathbf{r})$ has been obtained, properties of interest such as total energies and elastic constants may, in principle, be calculated. Though our primary interest is in the total energy of either bulk(§3.2.3), surface(§3.2.4) or interface(§3.2.5) systems, charge density maps (which illustrate the spatial distribution of electronic charge) and the density of states (DOS) plots are often useful in understanding the different bonding features.

There are several parameters that are used in the calculations. It is important that the calculations are converged with respect to these parameters – convergence is checked by ensuring that the properties of interest (such as the equilibrium lattice constant and/or the total energy) remain unchanged on changing the parameter concerned. Important parameters include the number of special k-points sampled in the Brillouin zone wedge and the number of interstitial plane waves.

The calculations are usually performed in the so-called atomic spheres approximation(ASA) to minimize the extent of interstitial region. Within the ASA, the muffin tins are overlapping spheres centered at every atom site, their size being determined by the constraint that the total system volume be occupied by these spheres.

3.2.3. Bulk calculation

Bulk calculations are required for providing input to subsequent surface or interface calculations. The first step, defining the direction of layer-partitioning, is often dictated by a subsequent surface/interface calculation which is of interest – for instance, if the aim is to calculate the surface energy of a (100) plane, then the system (both for the bulk and the surface calculation) is built by stacking (100) planes. The lattice constants determine the size of the 2-D cell in each layer and the inter-layer spacing.

A single calculation involves the *self-consistent* computation of the crystal potential and the total energy of the system at a given lattice constant. For this purpose, an iterative self-consistent field approach is usually adopted. Here, one starts with an initial input potential (which is usually obtained for a multi-atom unit cell from a simple superposition of individual atomic potentials) and obtains as output the electronic wavefunctions (and therefore the charge density) from the Schroedinger's equation; the available energy levels in the solid are filled up, in accordance with the Aufbau principle, starting from the lowest levels until all the electrons (which is fixed for a given system) have been accounted for. The highest occupied energy level represents the Fermi energy, E_f. The charge density is used to construct a new crystal potential which is compared with the input potential. If the difference is more than a preset tolerance, another iteration is started using a mixture of the old and new potential as the input potential. Otherwise, the potential is considered to be converged self-consistently and the energy of the system corresponding to the converged potential is then called the 'total energy' of the system. For calculations reported here, the total energy differences between successive iterations is less than a milli-Hartree (1 Hartree = 27.2 eV).

The value of the lattice constant is then varied and the self-consistency cycle repeated until a minimum is found in the corresponding total energy. The total energy is plotted as a function of the atomic volume, Ω (defined as V/N where V is the volume of the unit cell and N is the number of atoms per unit cell). An energy-volume relationship is obtained by fitting the data to the Birch-Murnaghan equation of state:

$$E(\Omega) = \sum_{n=0}^{N} a_n \left(\Omega^{-2/3}\right)^n \qquad (3)$$

where a_n is the expansion coefficient for order n. The equilibrium atomic volume (and hence the equilibrium lattice constant) is found by setting $dE/d\Omega$ equal to zero. The bulk modulus is calculated from the curvature of the E-Ω curve. Once the equilibrium ground state has been found, *charge density maps* and the *electronic density of states* (resolved by atomic sites and by angular momentum) at the equilibrium lattice constant can be easily generated.

3.2.4. Surface calculation

Of primary interest in a surface calculation is the determination of surface energy. A schematic of the setup for a typical surface calculation is shown in Figure 1. The free surface is simulated by using vacuum layers on top of a surface region that is defined such that all the layers inside the region feel (which is reflected by a crystal potential that is different from the bulk) the presence of the surface. The layers below the surface region constitute the bulk and are represented in the calculation by a single bulk layer. The crystal potential of this layer, identical to the converged potential from a bulk calculation, is held fixed and represents a boundary condition in the calculation. The Fermi energy of the surface system is given by that of the underlying bulk phase and the potential in the surface layers is allowed to relax subject to the boundary conditions imposed by the bulk potential and the Fermi energy. Unlike certain force calculations where the atom positions are moved at the end of every iteration, the atomic positions are held fixed in LKKR calculations. The converged total energy per 2-D unit cell, E_s, of this surface system includes the corresponding surface energy, γ, which is given by

$$\gamma = (E_s - mE_b)/\Delta \qquad (4)$$

where

E_b – energy/2-D unit cell of the bulk phase,

m – number of layers in the surface region, and

Δ – area of the 2-D unit cell

To ensure internal consistency, the number of vacuum layers and the number of surface layers are varied until the surface energy of the system does not change appreciably with a change in the number of either the vacuum or the surface layers. The surface energy is then said to be converged to its equilibrium value.

3.2.5. Interface calculation

The interface energy associated with a given interface can be obtained from an interface calculation which can be set up in one of two ways, both of which are illustrated in Figure 2. All interface calculations consider an interfacial region bound on either side by layers representing bulk systems. In the A|B type structure, there is one interface between the two phases and the

system is bound on one side by bulk A and on the other side by bulk B. In the sandwich structure, one of the phases (the minority phase) is entirely within the interfacial region which is bound on both sides by the same bulk phase (the majority phase). There are two interfaces between the two phases in this configuration. We have performed all our calculations in the sandwich structure as it more closely resembles an inclusion phase embedded in the matrix. We confine further description to the sandwich structure only.

Let A be the *bulk* bounding phase (typically represented by a layer on each side) and let there be m layers of phase B enveloped in n layers of phase A on either side. Then the complex of m+2n layers constitutes the interfacial region and the layers in it are called the interfacial layers. The Fermi energy of bulk A is imposed on the entire interfacial system, and the potential in the interface layers is allowed to relax, subject to the criterion that the system conserves the total number of electrons. Since this system contains two interfaces between A and B, the total energy includes twice the A|B interfacial energy. The interfacial energy, $\varepsilon_{A|B}$, is obtained from,

$$\varepsilon_{A|B} = (Etot - 2nE_A - mE_B)/(2\Delta) \quad (5)$$

where

E_{tot} – total energy of the interfacial system,

E_A, E_B – energy/layer of the respective bulk phases, and

Δ – area of the 2-D unit cell

As for the bulk and surface calculations, it is important to ensure the convergence of the calculations with respect to the number of interfacial layers in the two phases. This is accomplished by repeating the calculations with increasing n and m until there is no further change in the interface energy with increase in either m or n.

3.2.6. Work of adhesion

The surface and interface calculations yield the relevant surface and interface energies respectively, which when used in (1) yield the work of adhesion of a given interface. It is important to note that the W_{ad} so calculated is specific to the particular orientation and configuration of the interface including the relative orientation of the two phases and the inter-layer separation at the interface between the two phases.

4. Results and discussion

4.1. Experimental

4.1.1. Tensile properties

The tensile properties of the two heats are summarized in Table 2. The data represents the average of at least three specimens from each heat. Note that, while the heats have practically identical strength, the tensile ductility of the Ti_2CS heat is significantly higher than that of the MnS heat – this is indicative of a higher toughness for the Ti_2CS heat.

4.1.2. Particle characterization

Average particle size and volume fraction – The results of the SEM particle measurements are shown in Table 3. The particle size distribution for the two heats is shown in Figure 3. It can be seen that, in general, the Ti_2CS particles are smaller than the MnS particles and also that the size distribution is narrower for the Ti_2CS particles than for the MnS particles. Based on the assumption that all the sulfur present in the material is gettered as the inclusion of interest, the volume fraction of the inclusions has been estimated to be 0.000325 and 0.000533 in the MnS and Ti_2CS heats respectively. The measured volume fraction for the Ti_2CS heat is lower than the estimated volume fraction probably because of the smaller size of the particles – it is possible that some of the particles are smaller than the detection limit of the SEM and hence were not included in the volume fraction measurements. Subsequent TEM examination of thin foils did reveal the presence of particles smaller than 0.05μ in diameter. It is also possible that there may have been a few large (> 1μ) particles of Ti_2CS even though only 2-3 such particles were seen during the course of the present investigation. Such particles have been reported with a greater frequency in the UHS steels. In the case of the MnS heat, the discrepancy between the observed and the estimated volume fractions may be due to the inclusion of particles other than MnS (such as oxides or oxides-sulfides) in the measurements.

Morphology – It was possible to ascertain the shape and chemistry of large (diameter > 0.3μ) particles in the SEM, but for smaller particles, it was necessary to perform TEM studies on either thin foils or carbon extraction replicas. In the TEM, most of the particles observed in the MnS heat were in the 0.1-0.4μ dia. range, elliptical (in projection) with aspect ratio less than 2, and did not change shape upon significant tilting in the microscope – thus, it is fair to assume that most of the MnS particles are ellipsoidal, and by virtue of the small aspect ratio, fairly close to spherical. On the other hand, particles in the Ti_2CS heat were less than 0.2μ in diameter, and seemed to possess many different morphologies (Figure 4) with aspect ratios ranging from 1-4. It was

difficult to establish the exact 3-D shape of the particles, but it was clear that many particles possessed sharp edges and facets. From a void nucleation standpoint, it was interesting to investigate whether there was any morphology induced preference (such as plate faces, edges or corners) for void nucleation. In spite of the faceted morphology, the Ti_2CS particles did not seem to have any simple specific orientation relationships with the matrix. This suggests that perhaps a wide range of orientation relationships are possible between the Ti_2CS particles and the austenitic matrix.

Chemistry – The chemistry of the particles were mostly obtained from EDS spectra. As before, it was sufficient to use the SEM for larger particles, but it was necessary to use the TEM for smaller particles. However, the EDS unit attached to the TEM was not capable of detecting carbon, and Parallel Electron Energy Loss Spectroscopy (PEELS) was used to confirm the presence of carbon in the particles present in the Ti_2CS heat.

4.1.3. Void nucleation and growth

The processes of void nucleation and growth as a function of plastic strain were investigated using both SEM and TEM examination of tensile specimens that were either fractured or strained very close to fracture. The normalized void volume fraction as a function of plastic strain was obtained from SEM studies of the polished mid-plane cross-sections from the strained/fractured tensile specimens(§3.1.4.1). TEM studies were performed on foils (produced from thin slices parallel to the longitudinal mid-plane of the tensile specimens according to the procedure outlined in §3.1.4.2). The SEM and TEM studies were complementary in nature and together enabled a better comprehension of the void nucleation and growth processes than would have been possible had either of them been used in isolation.

4.1.3.1. SEM studies

MnS heat – There was considerable necking in the tensile specimens that were fractured or strained very close to fracture. Thus, regions of very high strain were confined to within 2-3mm of the fracture surface. The examination of specimens from the MnS heat in the optical microscope often revealed the presence of long extended voids near the neck in the heavily strained region. The voids were extended frequently along the tensile axis and at times close to the direction of maximum shear stresses (which are situated at 45° to the tensile axis). Closer examination in the SEM (Figure 5) revealed that these extended voids are actually compound voids, i.e. voids formed on several individual particles that had linked together. Many of these voids contained particles that were confirmed to be MnS by EDS analysis.

Quantitative measurements of the void volume fraction in the MnS heat were made from Polaroid pictures taken at 3000x magnification. The method used for void volume fraction measurement is identical to that used for particle volume fraction measurements. Seven frames close to the tensile axis were taken at each of the six strain levels (ranging from 0.27 to 0.85) examined. The specimen had a fracture strain of 1.55. A typical image obtained from the MnS heat specimen at a strain level of 0.85 is shown in Figure 6a. In the figure, the tensile axis is horizontal. The normalized void volume fraction was plotted as a function of plastic strain (Figure 7). Voids have begun nucleating when this ratio exceeds one. The nucleation strain is usually defined to be the strain near which the ratio begins to rapidly rise above 1. In the present case, it can be seen that the ratio is fairly flat until nearly a strain of 0.7 and then starts to increase, reaching a value of 3.44 for the highest strain level examined ($\varepsilon = 0.85$).

Ti_2CS heat – The necking in specimens from the Ti_2CS heat is similar to that for specimens from the MnS heat except being slightly more severe due to the higher fracture strain for the Ti_2CS heat relative to the MnS heat. Like for the MnS heat specimens, the heavily strained region is confined to 2-3mm from the fracture surface for the Ti_2CS heat also. Under the optical microscope, the strained/fractured Ti_2CS heat specimen revealed the presence of voids only very close (less than 0.5mm or so) to the fracture surface even at magnifications of 200x or higher. Only occasionally were the voids seen at locations farther away from the fracture surface. Otherwise, the specimen had an appearance similar to that of an unstrained specimen. The extended voids that were often seen in the MnS heat specimens were rarely seen in specimens from the Ti_2CS heat. As the highly strained region just below the fracture surface is in an advanced stage of void growth and coalescence, this observation suggests that there might be fundamental differences in the way void growth and coalescence occur in the two heats. The absence of long extended voids in the case of the Ti_2CS heat was further confirmed by low magnification (< 1000x) examination in the SEM. Even at magnifications of 3500x, it was difficult to find particles with large voids at strain levels as high as 85% of the fracture strain.

While initial qualitative observations of the strained specimens were performed using the CamScan SEM, the void volume fraction data for the Ti_2CS heat was obtained using an XL-30 field-emission gun (FEG) SEM manufactured by Philips. As the microscope was changed, it was decided to repeat the bulk volume fraction measurements for the Ti_2CS heat. An unstrained sample was prepared as before and 30 random frames were captured at a magnification of 5000x. The volume fraction obtained from this experiment was 0.000132, compared to the 0.000301 obtained previously. The new size distribution showed particles to be in the 0.04-0.20μ diameter range, similar to the earlier measurement. However, the presence/absence of occasional large

particles(~ 1μ diameter) was found to significantly alter the volume fraction. For instance, the presence of only 2 such large particles in the 30 frames examined would have led to the volume fraction being close to the earlier value obtained. As these large particles are very few in number, it is difficult to observe these in the SEM on a regular basis. Nevertheless, the normalized void generation data for the Ti_2CS heat was obtained using both the *old* and the *new* bulk volume fraction measurements. However, as the latter is smaller and therefore results in a more severe measure of void growth (which is likely an overestimate of the real void growth in the material), it is used for further analysis.

Twenty random frames each were captured at strain levels of 1.7, 1.5, 1.0 and 0.58 using a magnification of 4500x. The specimen had a fracture strain of 2.07. In addition, nine frames were captured from a strain level of 0.30 which was only slightly higher than the uniform strain. The void(+ particle) area fraction was determined for the different strain levels. The normalized void volume fraction as a function of strain is shown in Figure 7. The normalized void fraction data, computed using both the original bulk volume fraction and the 'new' bulk volume fraction, are shown. The normalized void volume fraction is not much different from 1 for strain levels less than 1.5. This data suggests that the nucleation strain is between 1 and 1.5. The normalized void volume fraction at a strain of 1.7 is 95; however, two very large voids are responsible for this large volume fraction – if these two voids are excluded, then the normalized volume fraction is reduced to 2.98. The data indicates that the void profusion strain, as defined previously, is greater than 1. It can also be seen that the void growth rate is rather low until fairly high (relative to the fracture strain) strains are reached. This is consistent with the earlier observation that even the highly strained regions (Figure 6b) in the Ti_2CS heat have a remarkably similar appearance, at least qualitatively, to the unstrained specimens and therefore should yield a normalized void volume fraction that is not much higher than 1.

Comparison between MnS and Ti_2CS heats

It can be seen (Figure 7) that the normalized void volume fraction starts to increase rapidly near a strain of 0.6-0.7 for the MnS heat; a similar increase for the Ti_2CS heat is not seen until the plastic strain is above 1-1.2. This behavior is similar to that observed in the UHS steels. It has been believed that the differences between the two heats is due to the better void nucleation resistance of the Ti_2CS particles.

4.1.3.2. TEM observations of void nucleation

The foils were loaded onto a double-tilt specimen holder such that a definite relationship existed between the y-axis (i.e. the transverse axis corresponding to the y-tilt) of the holder and the tensile axis on the specimen – often, the specimens were loaded such that the tensile axis is

parallel to the y-axis of the holder. When the relative orientation between the tensile axis and the specimen holder's y-axis is known, the orientation of features such as the particle poles (the term "particle pole" is used throughout to refer to either end of the particle along its major axis) and the void axes with respect to the tensile axis can be easily determined as follows: after locating the feature of interest, if the specimen's z-position is made to lie *off* the *eucentric-height* position, a rotation about the x-axis (the long axis of the specimen holder) at zero y-tilt will result in the features tracing a path on the screen parallel to the y-axis of the holder. As the tensile axis is positioned at a definite orientation to the y-axis, it should be possible to relate the orientation of the features to the tensile axis. The particles observed on the foils were predominantly imaged at either one or both of two x-tilt positions, namely zero tilt and a tilt of 12°, the latter being the tilt position required for acquisition of an EDS spectrum. Other tilt positions were only occasionally used. It was deduced from EDS spectra that except for 2-3 particles which were mixed oxide sulfides or oxides, the particles were mostly sulfides (MnS heat) or carbosulfides (Ti_2CS heat). Further, EELS analysis and elemental mapping were performed on particles found on the thin foil from the oversize Ti_2CS tensile specimen at a strain of 0.336. It was concluded that all of the observed particles were Ti_2CS.

For each particle observed, several parameters were measured to monitor the void nucleation and growth. The different measurements and the definitions of the parameters derived from these measurements are given below (see Figure 8 for an illustration):

Measurements

- d = projection along largest void
- d_1 = primary axis (usually this is parallel to or just off *d*)
- d' = minor axis (perpendicular to d_1)
- v_1, v_2 = void lengths along *d* on <u>either *side*</u> of particle
- v_1', v_2' = void lengths along d' on <u>either *side*</u> of particle

Derived Parameters

- Particle size = $(d + d') / 2$
- Aspect ratio = d/d' if d > d'; else d'/d
- Primary void size = $(v_1 + v_2) / 2$
- Secondary void size = $(v_1' + v_2') / 2$
- **Void growth index**, VGI = $(v_1 + v_2 + d) / d$
- **Void to particle ratio** = $(v_1 + v_2) / d$ = VGI - 1

The primary void size is a measure of the void length along the longest void while the secondary void size is similar to the primary void size, but is the mean void length *orthogonal* to

the primary void. In most cases, a non-zero secondary void size would indicate that a large fraction of the particle-matrix interface has debonded. It was found that more than 80% of the particles observed had a value of zero for the secondary void size indicating that void nucleation and growth was confined to regions close to the primary void. The **void growth index** (VGI) is the most important parameter in this analysis – voids have nucleated on the particle when VGI exceeds 1, and larger values of VGI imply a larger extent of void growth. It must be mentioned that the ion-milling step would likely open up large voids and therefore the VGI observed will be an overestimate of the actual void size for particles with large voids. However, the error would decrease with decreasing void size and the observed values should be quite accurate at the lower end of the VGI scale. The over-estimation of void growth for larger voids can be expected to be similar for voids at particles of both heats and therefore should not affect the comparison between the two heats.

4.1.3.2.1. MnS and Ti_2CS heats

MnS heat

A total of 23 particles comprising four different strain levels were observed for the oversize MnS heat specimen and 14 particles from 4 strain levels were observed for the regular MnS specimen. All but one of these 37 particles had nucleated voids. This suggests that almost all particles, at least amongst the particles observed, nucleate voids even at low strain levels such as 0.24.

Ti_2CS heat

In the Ti_2CS heat, 25 particles (3 different strain levels) and 10 particles (2 different strain levels) were observed in the oversize and the regular specimens respectively. Overall, the strain levels examined ranged from 0.323 to 1.000. In this case also, only one particle was found that had not nucleated a void. Thus, it appears that the void nucleation strain (as observed in the TEM) is fairly low (< 0.3) even for the Ti_2CS particles.

4.1.3.2.2. Size and shape of the observed particles

The particles observed for the MnS heat were 0.07-0.37μ (average = 0.227μ) in diameter with aspect ratios ranging from 1.0 to 2.5; however, more than 70% of particles had aspect ratios less than or equal to 1.2. Thus, a large number of the MnS particles observed on the TEM were fairly equiaxed or spherical. In the Ti_2CS heat, the particles were smaller with nearly 95% below 0.25μ (average = 0.170μ) in diameter. In general, the Ti_2CS particles had higher aspect ratios (ranging from 1 to 4) with at least 20% of the particles having aspect ratios greater than 2 and only 50% having values less than or equal to 1.2. At least 50% of the particles had sharp facets (at the

observed magnification which ranged from 82000x to 105,000x). The size-related features (size range, average size, aspect ratio etc.) of the voided-particles observed in the *strained* foils[1] of both heats were similar to those of the respective unstrained foils. This suggests that the void nucleation process does not preferentially seek out particles in a specific size range or with a certain aspect ratio.

4.1.3.2.3. Orientation of voids with respect to tensile axis

It was of interest to find the relative orientation of the voids with respect to the tensile axis and in the case of faceted particles whether there were preferred sites (like edges, corners or faces) for void nucleation and growth. The results of the present study show that the most dominant factor in determining the location of the nucleating void and the direction of void growth is the tensile axis (which is the direction of maximum tensile stresses). Voids nucleated at the particles in such a way that the maximum direction of growth of the void was parallel or close to the tensile axis. Voids were observed to have nucleated away from the main particle pole axis[2] and towards the tensile axis (Figure 9a). This was true, in general, for both the MnS and the Ti_2CS heats. However, if a facet or a particle pole was oriented at or near 45° to the tensile axis (and therefore parallel to the direction of maximum *shear* stresses), then void nucleation and subsequent growth seemed to occur at 45° to the tensile axis.

The presence of facets, irrespective of the particle's aspect ratio, does not appear to have any effect on the position of nucleating voids other than the one mentioned above. Voids have nucleated at the edges of long slender particles as well as on entire facets (Figure 9b) whenever the normal to the facets are close to the tensile axis. However, when particles were present along a grain boundary, the boundary may influence void growth. (Figure 10a). In Figure 10b, the grain boundary is nearly parallel to the tensile axis and therefore it was not possible to estimate the influence of the boundary on void nucleation and growth.

4.1.3.3. Observations on void growth

Particles, from both heats, in different stages of void nucleation and growth (i.e with different values of VGI) are shown in Figure 11. The VGI data for all particles, from all specimens, is shown in Figure 12a. Voids had nucleated at almost all of the particles, even at low strain levels ($\varepsilon < 0.35$). At these lower strain levels, while the VGI for individual particles varied from 1 to 1.5, the average VGI at a given strain level (Figure 12b) was less than 1.3 for both the MnS and the Ti_2CS heats. In both heats, even though the average VGI for a given strain increased steadily with increasing strain (Figure 12b), only 20-25% of the particles observed overall had a VGI

[1] Or more strictly, foils from strained specimens

greater than 1.5. Further, the data from all the four specimens seem to fall on one curve except that for the regular MnS heat specimen at a strain of 0.9 (VGI = 1.16) where the VGI would have been expected (based on the curve) to be in the 1.6-1.8 range. It is not clear as to why the average VGI for this foil is so low – it might be that the voids on some particles had become quite large leading to their *falling out* during specimen preparation.

4.1.4. Reconciling SEM and TEM void nucleation results

The SEM void generation data for the austenitic steels suggests a void nucleation strain of approximately 0.7 for the MnS heat and 1.2 for the Ti_2CS heat. In the MnS heat, the normalized void fraction for strains below 0.4 is less than two and is about 3.5 at a strain of 0.9. For the case of the Ti_2CS heat, the normalized void fraction is quite close to 1 for strains below 1.2, and is ~2.4 for a strain of 1.5. These observations suggest that significant void nucleation should not occur at strains below 0.7 for the MnS heat and below 1.0 for the Ti_2CS heat. This implies differences in the void nucleation behavior between the two heats.

TEM void nucleation data suggests that, in both the heats, voids nucleate at particles at strain levels much lower than what would have been expected based on the SEM results. The differences between the SEM and the TEM results are likely due to the differences in the capabilities of the two techniques.

In an SEM, the usual working magnifications for void or inclusion volume fraction studies (for the inclusion sizes found in the UHS steels and in the present study) range from 3000x to 5000x. At these magnifications, it is extremely difficult, if not impossible, to study particles or voids that are smaller than 0.05μ (an approximate order-of-magnitude estimate). For instance, any void nucleation on a particle that is 0.04μ in diameter would go undetected. In the back-scattered imaging mode, both the particles and the voids have identical contrast[3] and it is not possible to distinguish a particle inside a void unless the particles are large (> 0.3-0.4μ in diameter). It may be possible to employ the secondary electron imaging mode to distinguish particles and voids for slightly smaller particle sizes, but even the SEI mode is unsuitable for particles below about 0.10μ in diameter. Due to this inability to distinguish between particles and voids in the SEM, it is unfeasible to directly observe the early stages of void nucleation. One has to rely on the indirect measure of the normalized void+inclusion volume fraction to decide whether voids have nucleated or not.

---

[2] The main particle pole axis is the direction parallel to the major axis of the particle

[3] Contrast in the back-scattered mode is provided by differences in effective atomic number of the region scanned. For most inclusions in iron-based materials, the effective atomic number is lower than that of the matrix. Due to the *absence* of material, voids have an effective atomic number approaching zero and therefore both voids and inclusions have identical contrast in iron-based materials.

In contrast, the magnification employed in TEM studies are at least an order of magnitude higher – it is common to find magnifications of 60,000x to 150,000x being used routinely. The high magnification studies in the TEM enable the detection of even small features with sizes below 0.10μ. In the present TEM study, voids as small as 0.005μ (5 nm) in length have been detected. When the TEM has been used to study void nucleation, it is possible to directly observe small voids on small particles and thus a TEM study is likely to predict a lower void nucleation strain than an SEM study. Senior et al. (Senior et al., 1986) performed a TEM study of nucleation and growth of voids at carbides in a martensitic 9Cr-1Mo steel. They found that voids had nucleated as early as a strain of 0.09 (fracture strain was 1.2). However, the particles in their study were $M_{23}C_6$ carbides and Cr_2N nitrides. The volume fraction of the precipitates in the normalized and tempered condition was 0.015 with an average diameter of 0.07μ. Moreover the carbides had preferentially precipitated at lath boundaries or as clusters in the lath interiors. These two factors could have significantly influenced the void nucleation at the particles in this material. Nevertheless, it is reasonable to assume that TEM techniques, with careful specimen preparation, would likely predict lower void nucleation strains than SEM methods.

The differences in the scale of observation could not only influence the detection of void nucleation, but void growth as well. The SEM normalized void volume fraction as a function of strain remains quite flat (and close to 1) upto a certain strain and then starts to rise rapidly. In the past, this strain has been referred to as the nucleation strain. However, it is possible that, given the inability of the SEM to detect small particles/voids , the 'nucleation' strain really refers to the strain at which detectable void growth begins. In other words, it is possible that, below the so-called nucleation strain, not only have voids nucleated at particles, but they have also grown to some extent which is less than the detection limit of the SEM. Naturally, this effect would be more severe for the Ti_2CS particles which are considerably smaller than the MnS particles. Therefore, voids at Ti_2CS particles would not be detected until much larger levels of strain, as compared to those at MnS particles. This would imply that the normalized void volume fraction for the Ti_2CS heat would remain close to 1 until strains higher than those for the MnS heat, leading to a *higher* 'nucleation' strain being predicted for the Ti_2CS heat. Therefore, it could be argued that the so-called nucleation strain does not really refer to the actual void nucleation event, but instead refers to the strain beyond which significant void growth occurs so as to enable easy detection in the SEM.

The question then arises as to whether, once nucleated, voids grow at both MnS and Ti_2CS particles at the same rate. The present TEM VGI data indicates that this is the case. However, due to the limitations of the TEM technique explained previously, this may not be an accurate

depiction of the real situation. Presently, based on available data, no inferences can be drawn regarding the void growth behavior at the two different particle types.

Nevertheless, when the above factors are taken into account, it can be seen that the difference in the scale of observation between the SEM and the TEM could explain the observed disparities with respect to void nucleation and early growth at MnS and Ti_2CS particles. The SEM and TEM data are not really in conflict, but complement one another. The TEM technique is appropriate for detecting void nucleation (and perhaps early growth) while the SEM technique is ideal for examining significant void growth, and possibly coalescence.

4.2. Computational

The calculations necessary to determine the work of adhesion at a γ-Fe/MnS interface are described in detail(§4.2.1) in this report. While several calculations were performed and thoroughly analyzed(Ramalingam, 1998), the lack of space prevents all of them from being presented here. However, as the present work is probably the first to address the electronic structure and bonding in Ti_2CS, the results of calculations on bulk Ti_2CS are also presented in some detail(§4.2.2) – this would serve to illustrate how the electronic density of states and the charge density maps can be used to understand bonding. Finally, in §4.2.3, a summary of all the calculations performed in this work is presented.

4.2.1. Work of adhesion of a γ-Fe/MnS interface

When α-MnS (NaCl structure) precipitates in austenite, the following orientation relationship between the two phases is very likely:

$$(001)_{Fe} \parallel (001)_{MnS}$$
$$[110]_{Fe} \parallel [100]_{MnS} \qquad (6)$$

In order to obtain the work of adhesion at this interface, it is evident from (1) that the surface energies of the (001) surfaces of the two phases and the interface energy need to be computed. The atomic arrangement in the (001) planes of Fe and MnS are shown in Figure 13 and the orientation relationship at the interface is illustrated in Figure 14. Perfect lattice matching implies that, geometrically, $a_{MnS} = \sqrt{2}a_{Fe}$ for the interface calculation. The 2-D unit cell (shown shaded in Figure 14) used for the calculation has the dimension equal to a_{Fe} (= $a_{MnS}/\sqrt{2}$). In order to preserve consistency, the same 2-D unit cell was used for all bulk, surface and interface calculations. Also, all the calculations were done spin-polarized because MnS is a magnetic system even though γ-Fe is not.

4.2.1.1. Bulk calculations

The experimentally observed lattice constant for γ-Fe is 6.81 Bohr (1 Bohr = 1 a.u. = 0.529Å). The total energy of the system was obtained self-consistently for a range of lattice constants in the vicinity of 6.8 a.u. until an energy minimum was found. The plot of total energy as a function of the atomic volume is shown in Figure 15. The equilibrium lattice constant was found to be 6.46 Bohr (corresponding to Ω_0 = 67.4938 Bohr^3) and the corresponding total energy was -2542.02035 Ha/2-D unit cell.

The k-point convergence of the equilibrium properties was ensured by sampling 10, 36 and 136 k-points in the irreducible zone wedge. The results of this study (Table 4) indicate that it is adequate to sample 36 k-points. Similarly, we have also ensured the convergence in the number of plane wave rings (Table 4). This was done by checking the total energy values at the equilibrium lattice constant of 6.46 a.u. Iron calculations are converged after the inclusion of 8 plane wave rings.

Likewise, we obtained a total energy-volume curve for MnS. The equilibrium lattice constant was found to be 8.70 a.u. However, we are ultimately interested in the Fe/MnS interface where $a_{MnS} = \sqrt{2}a_{Fe}$. To achieve this match, it was decided to change the lattice constant of MnS to correspond to the equilibrium lattice constant of iron. This is justified because the MnS phase has a lower bulk modulus than the Fe. Therefore, manganese sulfide with a lattice constant of 9.14 Bohr ($6.46\sqrt{2}$) was used for all subsequent calculations.

An additional bulk calculation is necessary in this case: the subsequent interface calculation requires the Fermi energy of both Fe and MnS to be that of bulk Fe; thus, it becomes necessary to reconverge the potential and the total energy of MnS (with lattice constant 9.14 a.u.) at the Fermi energy of bulk Fe. In this calculation, the Fermi energy is fixed and the potential is allowed to relax self-consistently while conserving the total number of electrons. The corresponding total energy was found to be -1555.44569 Ha/2-D unit cell.

4.2.1.2. Surface calculations

As mentioned earlier, the same 2-D unit cell that was used for the bulk calculations was used to perform the (001) surface calculations for both Fe and MnS.

MnS (001) surface – The surface calculation on the MnS system was carried out for a = 9.14 a.u. with E_f being set at that of bulk MnS with the same lattice constant. Self-consistent calculations were carried out to converge the potential and the total energy of the system which consisted of a few vacuum layers (to simulate the free surface) on top of several surface layers. The surface layers were attached to a layer representing bulk MnS. Initially, 2 vacuum layers and 4 surface layers of MnS were used. The surface energy was found to be 2.09 J/m^2. Then the

number of vacuum layers and MnS surface layers were varied to ensure convergence (Table 5). As for the bulk, plane wave convergence was also ensured for the surface calculations.

Fe (001) surface – A surface system similar to the MnS surface was used to compute the surface energy of γ-Fe . The (001) surface energy of iron, using two vacuum and four iron surface layers was found to be 2.57 J/m^2. This value compares favorably with those reported in the literature for fcc iron.

4.2.1.3. Interface calculation

The interface between Fe and MnS was constructed in the sandwich structure (§3.2.4). The Fermi energy for the system was fixed at that of bulk Fe ($\varepsilon_{F|Fe}$). The total energy of the system was obtained self-consistently and the interface energy computed using (5). Table 6 shows the interfacial energy as a function of the number of interfacial layers in the calculation – it can be seen that it is sufficient to include four Fe and seven MnS layers to simulate the interfacial region accurately. From our calculations, we have calculated the interface energy of the given system to be 1.52 J/m^2 (using 8 plane wave rings). The absence of any reports in the literature of either the surface energy of MnS or the interface energy of a Fe/MnS interface makes it difficult to assess the accuracy of the values we have obtained.

4.2.1.4. Work of adhesion

All of our calculations are well converged when using at least 8 plane wave rings; convergence with respect to the number of layers has been independently ensured for every surface and interface calculation. The following surface and interface energies have been obtained from calculations converged with all the important parameters: γ_{Fe} = 2.57 J/m^2; γ_{MnS} = 2.09 J/m^2 and $\varepsilon_{Fe|MnS}$ = 1.52 J/m^2. Using these values in (1), we obtain the work of adhesion of the interface to be 3.14 J/m^2.

It must be borne in mind that our calculations are performed at zero K, with no atomic relaxations and with the muffin-tin form of the crystal potential. Also, the calculation is suitable only for those orientation relationships where there is a good lattice matching between the two phases and where the bulk Fermi energy differences are small (less than 0.2 Ha). Within these limitations, our values seem reasonable, especially in comparison to similar calculations. However, we are not aware of any reports in the literature regarding either the surface energy of MnS or the work of adhesion of the interface. Under such circumstances, it becomes difficult to draw conclusions on the accuracy and reliability of our calculations. Thus we have to resort to indirect means to check the validity of our results.

First, it should be noted that in the ductile fracture literature it is common practice to regard particles of MnS in steels to behave as pre-existing voids. This suggests that the work of adhesion of the Fe/MnS interface should be regarded as very small and that the void enclosing an isolated particle of MnS would begin growing continuously with increasing plastic strain in accordance with the equations governing the growth of a single void such as the void growth law of Rice and Tracey(Rice and Tracey, 1969). However, Maloney found in uniaxial tension that voids were first nucleated at equiaxed MnS particles in HY180 steel at a plastic strain of 0.5 to 0.75 depending on the tempering condition(Maloney, 1992). Wojcieszynski investigated void nucleation at particles of MnS in uniaxial tension for the as-quenched microstructure of a 9-nickel martensitic steel(Wojcieszynski, 1993). He found that voids were first nucleated at a plastic strain of 0.3 to 0.4.

That it is observed that voids are not nucleated in uniaxial tension until plastic strains of about 0.3 to 0.75 suggests that particles of MnS cannot in general be regarded as pre-existing voids. However, it is generally accepted that the carbides are more strongly bonded to the matrix than are particles of MnS and are also more void nucleation resistant. Void nucleation at spheroidized iron carbides (cementite) in steel has been studied by a number of workers. Fisher and Gurland carried out experimental studies of void nucleation at spheroidized carbides for a number of steels and discussed the experimental results in the context of their model for void nucleation which is based on a "double-criterion for void nucleation at particle-matrix interfaces"(Fisher and Gurland, 1981a; Fisher and Gurland, 1981b). Their model requires that a critical stress be exceeded over some region of the particle-matrix boundary and also that the elastic strain energy released in forming a void-cap exceed the energy associated with the creation of the two free surfaces. The energy required to create the two free surfaces is proportional to the work of adhesion of the interface. Their model predicts that the tendency for void nucleation increases with a decrease in the work of adhesion. Based on thermodynamic considerations they take the work of adhesion of cementite/matrix interfaces to be 5.7 J/m^2 and this value of the work of adhesion when used in their model results in reasonable agreement with their experimental results and the predictions of their model.

Based on the above considerations, one would expect the work of adhesion at a sulfide/matrix interface to be greater than zero and less than the 5.7 J/m^2 given by Fisher and Gurland for a cementite/matrix interface. In this light, our value of 3.14 J/m^2 for the MnS/matrix interface seems reasonable. Furthermore, the work of adhesion for the MnS/steel interface is less than twice the surface energy of the (001) surface of MnS, 4.18 J/m^2. If the work of adhesion had been greater than this value, one might observe fracture of the MnS particles prior to decohesion

of the particle-matrix interface even at small particle sizes. Therefore, our computational results are in agreement with the experimental observation that void nucleation by particle fracture is not seen for small equiaxed particles of MnS.

4.2.2. Calculations on bulk Ti_2CS

There is scarcely any literature, either computational or experimental, on the properties of Ti_2CS. Besides the crystal structure and the lattice dimensions, very little is known about the phase. Ti_2CS has a hexagonal crystal structure (space group $P6_3/mmc$) with two formula units per unit cell (Figure 16). The lattice parameters have been determined, using electron diffraction patterns of particles present in steel (Kudielka and Rohde, 1960), to be the following: c = 11.2 Å, a = 3.21Å (c/a = 3.5) and z = 0.099. 'z' is an additional variable required for specifying the position of the Ti atoms. Each basal plane in the structure is occupied by only one chemical species, either Ti, C or S. The stacking sequence of basal planes is AMXMBMXMA..., where A and B refer to C planes, M = Ti and X = S. All the atoms in the structure are six-fold coordinated – while the carbon atoms are octahedrally coordinated by the metal atoms, the sulfur atoms are trigonal-prismatically coordinated by the metal atoms. This arrangement leaves the metal atoms in a *distorted* octahedral coordination, with the three carbon atoms being closer than the three sulfur atoms by about 14 per cent. This structure can also be perceived to be a hexagonal close-packed stacking (ABAB..) of sulfur planes with layers of carbon-centered metal octahedra inserted between adjacent sulfur planes. The octahedra are linked to one another by sharing edges that do not lie(six of twelve) in the basal plane. The sulfur atoms occupy trigonal prismatic sites between two layers of octahedra – half the trigonal prismatic sites are left empty in accordance with the stoichiometry.

While the nearest-neighbor coordination for C is octahedral (point group symmetry $m\bar{3}m$) as in TiC, the point group symmetry at the carbon site in Ti_2CS is actually lower, being $\bar{3}m$. The site symmetries at the Ti and the S sites are 3m and $\bar{6}m2$ respectively(Pearson, 1972). The Ti-C bond length calculated from the atomic positions is 2.160Å and the Ti-S bond length is 2.513Å. Table 7 shows the elemental bond length, and the covalent and ionic radii of Ti, C, and S as reported in the literature(Winter,). It is interesting to note that, in Ti_2CS, the Ti-C bond length corresponds quite well with the sum (2.13Å) of Ti and C covalent radii, while the Ti-S bond length is in agreement with the sum (2.52Å) of S^{2-} and Ti^{4+} ionic radii. This implies that, from a conventional bonding view point, two different radii (with a difference greater than 0.60Å) are required to describe the same Ti atom in its bonding with its two different neighbors. This suggests that simple bonding theories are incapable of adequately describing the bonding in

Ti_2CS. Thus, we have adopted a first-principles approach to investigate the electronic structure and bonding in Ti_2CS.

The atomic arrangement in Ti_2CS lends naturally to a layer-decomposition in which the uniatomic basal planes are stacked together to form the 3-D solid. The LKKR calculations were performed using the atomic spheres approximation with all the three atom types being assigned equal sphere radii. While the choice of non-equal sphere radii for the different atoms may be expected to produce better results for most systems, especially with regards to determining the ionic/covalent nature of the different bonds, it is not possible to assign reasonable, yet different, muffin tin radii to the titanium, carbon and sulfur atoms in Ti_2CS because of the need to describe the titanium atom by two different radii (as outlined in the previous section). The s, p, and d partial waves were included on all sites. The von Barth-Hedin(Barth and Hedin, 1972) local spin density functional was used in all calculations. The unit cell has eight layers and several degrees of freedom for atomic positions, making the calculations involving the carbosulfide quite complex and computer-intensive. In this work, only *a* (the lattice parameter in the basal plane) has been varied while c/a and z have been kept constant at the experimentally observed values of 3.5 and 0.099 respectively.

4.2.2.1. Equilibrium parameters

The variation of the total energy as a function of the atomic volume is shown in Figure 17. Initially, the calculations were done by sampling only 6 k-points in the irreducible 2-D Brillouin zone wedge and using 6 plane wave rings (equivalent to 37 interstitial plane waves for the geometry of the 2-D unit cell) – this predicted an equilibrium lattice constant of 6.25 Bohr and a bulk modulus of 2.5 Mbar. Subsequently, both plane-wave and k-point convergence were ensured. The predicted value of the lattice constant is about 3% higher than the experimentally reported value. Normally, the LKKR calculations predict the lattice constant to within 3%. Empirically, it has been found that the predicted values are typically lower than the experimentally reported values, at least for simple systems. While it is known that "exact" (full potential) local density approximation (LDA) has a tendency to overbind (resulting in smaller equilibrium lattice constants), "approximate" LDA may not, especially for non-simple systems such as Ti_2CS. Nevertheless, the current results seem to be quite reasonable. The bulk modulus of Ti_2CS falls in the range of the bulk modulii of the transition metals(Moruzzi et al., 1978); however, given the nature of the species involved, one should not expect the bonding in Ti_2CS to be entirely, or even predominantly, metallic. That the bulk modulus of Ti_2CS also happens to be

intermediate to those of typical ionic and covalent materials[4] seems to suggest the presence of complex bonding involving covalent, ionic and metallic features.

4.2.2.2. Density of states

The total and the site-resolved density of states (DOS) in Ti_2CS are shown in Figure 18 and Figure 19 respectively. The angular momentum resolved DOS for the different sites are shown in Figure 20. The total DOS (Figure 18) can be conveniently divided into five zones for discussion: (a) The lowest lying valence band occurs around -15 eV and is essentially due to the sulfur 3s states. There is an energy gap of about 3eV following this band. (b) A narrower band of carbon 2s states occurs at about -9 eV. (c) The S 3p states dominate the DOS in a rather broad range from -8eV to -3eV and there is a small contribution from both Ti (d-levels) and C (p-levels). (d) Just below the Fermi energy are the bonding p-d hybrids, predominantly C 2p and Ti 3d, with peaks at -3eV and -2eV. (e) Near the Fermi level, a small peak due to the Ti 3d states is observed. Just above the Fermi level, most of the contribution to the DOS comes from the unhybridized Ti 3d states. The anti-bonding p-d hybrids dominate the DOS occur in the vicinity of 5eV(see also figure 6). Several interesting features can be noted:

Firstly, the fact that the peaks of the 2s and 2p bands originating from carbon are well separated (about 7eV, Figure 20) indicates that there is no sp^3 hybridization of the carbon valence orbitals; while the sp^3 nomenclature is that of valence bond theory and not molecular orbital theory, such a hybridization nevertheless would result in all s- and p- orbitals (bands) being in the same energy range without any gaps between them(Cottrell, 1995). That this is not the case in Ti_2CS precludes any sp^3 hybridization. This is further supported by the fact that, in general, sp^3 hybridized systems prefer a four-fold tetrahedral coordination (as in diamond for instance) than any six-fold coordination (like an octahedron or a trigonal prism).

Secondly, there is significant p-d hybridization between the Ti d-states and the non-metal (mainly, but not entirely, C) p-states – that this is so is suggested (Figure 20) by the presence of simultaneous peaks for Ti-3d and S-2p at -5.5eV, and for Ti-3d and C-2p at both -3eV and -2eV; these can be interpreted to be the bonding p-d hybrids. The corresponding anti-bonding hybrids for the Ti-C bond are located about 5eV above the Fermi level (Figure 20). This is similar to the situation in TiC(Cottrell, 1995) where the band split is 7eV between the bonding and the anti-bonding p-d hybrids. A comparable band split in Ti_2CS indicates that the Ti-C bond in this system is similar to the Ti-C bond in TiC. This is also supported by the fact that the Ti-C bond

[4] for instance, while the alkali halides (the prototypical ionic solids) have a bulk modulus less than 1Mbar (Harrison, 1988; Kumar, 1995), the calculated bulk modulus for diamond (a covalent solid) is about 4.50

lengths in both TiC(Cottrell, 1995) and Ti_2CS are nearly identical. Our calculations on TiC (Ramalingam, 1998) also confirm this.

It is also interesting to note that the Ti-Ti distance is shorter across the carbon plane than in the same (basal) plane. Thus any significant d-d interaction involving the Ti atoms will have to occur across the carbon plane and hence this interaction can be expected to be weak (owing to the carbon mediation; also, the Ti-C and the Ti-S bond lengths are shorter than this Ti-Ti distance), relative to the direct Ti-Ti bonding such as can be found in metallic Ti for instance – in the latter, most of the binding energy of the solid comes from the d-d bonding between Ti atoms, whereas in the case of Ti_2CS (and TiC), this has largely been replaced by the p-d bonding between the non-metal and the metal atoms. That the d-d interaction in Ti_2CS is (relatively) weak can be seen from the high density of d-states (Figure 20, panel for the Ti d-band) just above the Fermi level and confined to a small energy width, indicating localization and an almost negligible overlap of the d-orbitals under consideration. Coupled with a finite DOS at the Fermi energy, this leads to the electronic conductivity of Ti_2CS being metal-like – in this respect also, the carbosulfide resembles the monocarbide.

4.2.2.3. Charge density maps

The spatial distribution of the valence charge density was investigated by plotting the charge density in several different crystallographic planes. The most informative of these, plotted in the $(11\bar{2}0)$ and several (0001) type planes, are shown in Figure 21 and Figure 22. The contours are in units of electrons/Bohr^3 and the units have been omitted in the following discussion for clarity. The $(11\bar{2}0)$ plane (a prism plane) contains all three atom types and was chosen because of our interest in analyzing the Ti-C and the Ti-S bonding – the different energy ranges were chosen based on interesting features in the electronic DOS (Figure 18). As shown in the schematic (Figure 21a), the vertical direction is parallel to [0001] (the c-axis) and the horizontal direction is parallel to $[1\bar{1}00]$, which is the longer of the two face diagonals of the unit cell in the basal plane. The distance between successive carbon atoms along the vertical direction is c/2 and that along the horizontal direction is $a\sqrt{3}$. The charge density in the (0001) planes (Figure 22b-d) has been included to facilitate interpretation of some of the features seen in the plot of the density in the prism plane. As expected, large distortions can be seen in the distribution of charge around the atoms.

Mbar (Hebbache, 1999; Lundin et al., 1998). The calculated bulk modulus of TiC is 3.49 Mbar (Gubanov et al., 1994).

It can be seen from the DOS (Figure 20) that the p-band due to sulfur occurs in the range -8 to -2 eV, with the primary peak just below -5eV, while the carbon p-band is more localized (-5 to -1 eV) with the main peaks near -3eV and -2eV. The first two energy ranges shown in Figure 21, namely -6.5eV to -4.5eV(Figure 21b) and -3.5eV to -1eV (Figure 21c), were chosen to incorporate the main peak(s) of the sulfur and the carbon p-bands respectively. The contribution of the Ti d-states to the former is relatively small compared to the latter (Figure 20), and this is reflected in the charge density distribution in the vicinity of the Ti atoms in the two panels. In the former, while the charge on the Ti has shifted towards the sulfur plane (as seen in the 0.05 contour for example), there is actually a region of very low density along the line joining the Ti and the sulfur atoms. Also, large areas in the plane (white regions) have very low charge density (values < 0.01). In the -3.5eV to -1eV range, the 0.05 and the 0.10 contours on Ti have been drawn *towards* the carbon atom, while the 0.05 contours on sulfur appear to be stretched along the horizontal direction on one side only. This 'stretching' is a manifestation of the drawing of charge towards the titanium atoms at the edges of the trigonal prism, and not of a bond between in-plane sulfur neighbors (see later discussion on Figure 22). Note also that this energy range represents a region of higher charge density than the previous range, in that the 0.03 contour wraps around all three atom types and that there is a significantly smaller area with charge density less than 0.01. The orbitals on the Ti atoms are oriented in an unfavorable fashion for any metal-metal interaction, leading to regions of very low charge density along the line joining nearest-neighbor Ti atoms.

The other two energy ranges, namely -1eV to +1eV (Figure 21d) and 1eV to 4eV (Figure 22), were chosen to analyze the metal-metal bonding. Unlike the situation in the -3.5eV to -1eV range, the d-orbitals on Ti are now oriented favorably for nearest-neighbor metal-metal interaction, with the carbon mediation being very evident in the -1eV to +1eV range. In this range, there is still substantial C-Ti bonding present along with Ti-Ti bonding – the 0.10 charge contour (Figure 21d) suggests inter-linked C-Ti_6 octahedra with charge clearly being piled up in the C-Ti and the Ti-Ti bonds. Here, the asymmetry between the left and the right lobes of charge density (with respect to the 0.05 and the 0.10 contours) on the sulfur atoms is a result of the charge moving away from the Ti atoms, unlike the situation in the 1eV to 4eV range where the charge is concentrated towards the Ti atoms (Figure 22,a and c).

The d-d type interaction between the Ti atoms is very evident when the charge density is plotted in the 1eV to 4eV range (Figure 22a). Line 1 (shown in the figure as joining two Ti atoms) is the same line shown in Figure 22b, which is the charge density in a (0001) plane passing through Ti atoms. The latter figure shows that the charge in the vicinity of the Ti atom is oriented

away from the carbon atoms in the neighboring plane and piled up towards the Ti atoms (marked with an X and equivalent positions) in the plane below the plane of carbon atoms. Similarly, line 2 (shown in Figure 22a as joining two sulfur atoms) is the same line shown in Figure 22c, which shows the charge density in a (0001) plane passing through sulfur atoms. The asymmetry in the lobes surrounding the sulfur atoms can now be clearly seen to be a preferential accumulation of charge towards the nearest-neighbor titanium atoms (position marked with 'X' in Figure 22c) at the corners of the trigonal prism. Note that the maximum charge in the (0001) type Ti, S and the C planes are 1.74, 0.60 and 0.10 respectively. While the charge density in the carbon plane is relatively low, one can clearly see (Figure 22d) the 'linking' (in the form of six elongated ovals surrounding every carbon atom) of the charge density lobes of the titanium atoms above and below the carbon plane.

4.2.2.4. Conclusions on bonding in bulk Ti_2CS

The electronic density of states of Ti_2CS is remarkably similar to that of TiC, and suggests that many electronic properties of Ti_2CS may be similar to that of TiC, including a metal-like electronic conductivity. The density of states and the calculated bulk modulus seem to suggest that there is complex bonding between Ti and its anionic neighbors exhibiting covalent, ionic and metallic features. The charge density, examined at different energy ranges and on different crystallographic planes, also supports this analysis

4.2.3. Summary of calculations on other systems

During the course of this work, it was realized that a γ-Fe/Ti_2CS interface could not be addressed using the present computational technique because there seems to be neither a simple orientation relationship nor a good lattice match at the interface. In order to mimic the γ-Fe/Ti_2CS interface, it was decided to compute the W_{ad} of a γ-Fe/carbide interface. While TiC was the most obvious choice to replace Ti_2CS, there was not a good lattice match and so ZrC was used instead. Both TiC and ZrC have the same crystal structure and atomic arrangements as MnS.

Thus, the other systems treated in the present work were bulk and (001) surfaces of TiC and ZrC. Besides, bulk bcc iron was also studied in order to verify whether the LKKR method adequately handled a *magnetic* system. The summary of results of these calculations is presented in Table 8. The negative work of adhesion that was obtained for the γ-Fe/ZrC interface was rather surprising – some possible reasons and consequences of this curious result are presented in §5.1.

5. Summary of present work

5.1. Interfacial bonding studies

The bonding studies were carried out using first-principles electronic structure calculations. It may be recalled that our original interest was in comparing interfaces of MnS and Ti_2CS particles with γ-Fe. However, as no good lattice matching[5] was present for a simple orientation relationship between Ti_2CS and γ-Fe, an alternative inclusion phase was chosen. The choice of ZrC was based on the facts that (a) bonding characteristics (such as the extent of ionic bonding) in Ti_2CS are in-between those of sulfides and carbides, and (b) TiC, the obvious carbide of choice, had poor lattice matching at the interface and could not be treated by the present method. In the literature, it has been postulated that carbides are more strongly bonded to a steel matrix than sulfide particles. In order to investigate this premise, interfaces of MnS and ZrC with an austenitic iron matrix and with simple orientation relationships at the interface were investigated. A planar interface was assumed to prevail in both cases with the following orientation relationship: $(001)_{\gamma\text{-Fe}} \parallel (001)_I$ and $[100]_{\gamma\text{-Fe}} \parallel [110]_I$ where 'I' represents the inclusion phase. The work of adhesion, a measure of the interfacial strength, was computed for the two different interfaces from calculations that were performed on the appropriate bulk, surface and interfacial systems.

γ-Fe/MnS interface

In the γ-Fe/MnS system, the surface energies of γ-Fe and MnS have been found to be $2.57 J/m^2$ and $2.09 J/m^2$. The interfacial energy of the γ-Fe/MnS interface has been determined to be $1.52 J/m^2$ leading to a work of adhesion of $3.14 J/m^2$. The work of adhesion is significantly higher than zero suggesting that inclusions of MnS cannot be regarded as pre-existing voids (as has often been done in the void nucleation literature).

γ-Fe/ZrC interface

In the γ-Fe/ZrC system, while the surface energies of γ-Fe and ZrC are $2.57 J/m^2$ and $1.79 J/m^2$ respectively, the interfacial energy between the two phases has been determined to be greater than $8 J/m^2$. This unusually high value of the interface energy leads to the work of adhesion being nearly $-4 J/m^2$. This would imply that the interface is highly unstable and would spontaneously decohere to expose the free surfaces of γ-Fe and ZrC. This result is very surprising given the belief that the carbides are more strongly bonded to the matrix than sulfides which would lead one to expect the work of adhesion at the γ-Fe/ZrC interface to be higher than $3.14 J/m^2$, the value

[5] The calculations can handle only systems with a simple orientation relationship and good lattice matching at the interface

obtained for the γ-Fe/MnS interface. The unanticipated nature of the present result necessitated a few more calculations on the γ-Fe/ZrC interface in which different parameters were varied – in all of these calculations, while deviations from the earlier value were seen, the interface energy continued to be rather high (> 5.5J/m^2) leading always to a *negative* value for the work of adhesion.

If the present results are true, then it casts serious doubts on the conventional belief about the carbides being more strongly bonded to the matrix than the sulfides. The notion regarding the adhesion of carbides to the matrix is not based on interfacial energy data, but comes from experimental observations of void nucleation at the two particle types during the different stages of fracture – the sulfides have always been observed to nucleate voids earlier than the carbides. There are several possibilities as to why the above conclusion about the bonding of carbides to the matrix may be invalid: (a) It may be that the conclusions were very much due to the scales of observation. The carbides are typically much smaller than the sulfides – as most of the earlier studies on void nucleation at carbides were carried out either in the optical microscope or in the SEM it is likely that small voids at these carbides would not have been detected. (b) It may be that the carbides are not well bonded to the matrix, but factors other than interfacial bonding dominate the void nucleation process. (c) It may also be that the carbides have nucleated voids but void growth rates at the carbides are much lower than those at sulfides either due to their small size or due to their non-spherical shapes.

On the other hand, it may well be that some of the assumptions that have been used in the present calculation are not entirely valid. Presently, with the available data, it is not possible to determine the causes of discrepancy between the observed (calculated) and the expected behavior of the γ-Fe/ZrC interface. Nevertheless, this issue has important ramifications for the understanding of void nucleation and growth at different inclusion/matrix interfaces and needs to be addressed in the future.

5.2. Void nucleation and growth studies

The void nucleation and growth at MnS and Ti_2CS inclusions in a model austenitic steel were investigated both by SEM and TEM methods. Two heats of the austenitic steel, one containing MnS inclusions and the other containing Ti_2CS particles, were used in the present work. Mechanical property data were obtained from tensile tests on axisymmetric specimens. The SEM studies were performed on polished longitudinal mid-plane sections of fractured[6] tensile specimens from both the heats. The TEM studies were done on thin foils obtained at different

[6] Or strained close to fracture

levels of strain from tensile specimens that had been strained to fracture. The main observations from these investigations are the following:

SEM normalized void volume fraction data suggests a void profusion strain of about 0.7 and 1.2 for the MnS and the Ti_2CS heats respectively. This behavior is similar to that observed in the UHS steels.

TEM observations indicate that void nucleation occurs at fairly low strains (~ 0.35) at both MnS and Ti_2CS particles.

TEM void growth data, as monitored by the void growth index (a normalized void length), suggests that no differences exist, at least for the strain levels examined, between the MnS and the Ti_2CS heats.

The tensile ductility of the Ti_2CS heat is higher than that of the MnS heat. The higher tensile ductility is consistent with higher ductility when sulfur has been gettered as Ti_2CS in HY180 and 9Ni steels.

The void growth and coalescence behavior during the terminal stages of the fracture process appear to be different, at least qualitatively, for the Ti_2CS and the MnS heats – much smaller extents of void growth and coalescence are seen in the case of the Ti_2CS heat even at strains that are close to the fracture strain. This result is very difficult to rationalize with (b) above unless void growth and/or coalescence are very different in the two heats.

In the UHS steels(Maloney, 1992), based on the SEM normalized void volume fraction data, the higher tensile ductility of the Ti2CS heat has been attributed to its larger void nucleation strain (as compared to the MnS heat), which in turn, has been believed to be due to the better void nucleation resistance of the Ti_2CS particles.

The present TEM observations suggest that the void nucleation strains are much lower, for both the MnS and the Ti_2CS heats, than those suggested by the SEM void volume fraction data. This implies that the higher tensile ductility of the Ti_2CS heat cannot be attributed to higher void nucleation strains (and in turn, to a better void nucleation resistance) in the Ti_2CS heat, at least in the austenitic steel used in the current study.

Further, as indicated by the VGI data, the void growth rates at both MnS and Ti_2CS particles appear to be similar. However, as discussed previously, this may be due to limitations in the TEM technique, especially the inability to investigate particles associated with large VGI values. In reality, the void growth behavior of the two heats may be quite different. Qualitative SEM observations suggest that differences may exist, between the MnS and the Ti_2CS heats, in the void growth and coalescence stages of the fracture process. These differences may be responsible for the differences in tensile ductility of the two heats.

6. References

Ashby, M.F. and Ebeling, R., 1966. Transactions of the AIME, 236: 1396.

Barth, U.v. and Hedin, L., 1972. Journal of Physics C: Solid State Physics, 5(1972): 1629-1642.

Cottrell, A., 1995. Chemical Bonding in Transition Metal Carbides. The Institute of Materials, London, 97 pp.

Fisher, J.R. and Gurland, J., 1981a. Metal Science(May 1981): 185 - 192.

Fisher, J.R. and Gurland, J., 1981b. Metal Science(May 1981): 193 - 201.

Garrison, W.M. and Moody, N.R., 1987. Journal of Physics and Chemistry of Solids, 48(11): 1035 - 1074.

Gubanov, V.A., Ivanovsky, A.L. and Zhukov, V.P., 1994. Electronic structure of refractory carbides and nitrides. Cambridge University Press.

Handerhahn, K.J., 1987. The effects of microstructure on the crack initiation toughness of high strength secondary hardening steels. Ph.D. Thesis, Carnegie Mellon University, Pittsburgh.

Handerhan, K.J., Garrison, W.M. and Moody, N.R., 1989. Metallurgical Transactions A, 20A(January 1989): 105 - 121.

Harrison, W.A., 1988. Electronic structure and the properties of solids: The physics of the chemical bond. Dover, New York.

Hebbache, M., 1999. Solid State Communications, 110(1999): 559-564.

Kudielka, H. and Rohde, H., 1960. Zeitschrift fuer Kristallographie, KristallPhysik, KristallChemie, 114: 447.

Kumar, M., 1995. Physica B, 212(1995): 391-394.

Lundin, U. et al., 1998. Physical Review B, 57(9): 4979-4982.

MacLaren, J.M., Crampin, S., Vvedensky, D.D. and Pendry, J.B., 1989. Physical Review B, 40(18): 12164-75.

Maloney, J.L., 1992. The Effect of Primary Void Nuclei on the Fracture Initiation Toughness of Ultra High Strength Steels. Ph. D. Thesis, Carnegie Mellon University, Pittsburgh, 492 pp.

Maloney, J.L. and Garrison, W.M., 1989. Scripta Metallurgica, 23: 2097 - 2100.

Moruzzi, V.L., Janak, J.F. and Williams, A.R., 1978. Calculated electronic properties of metals. Pergamon Press.

Pearson, W.B., 1972. A Handbook of Lattice Spacings and Structures of Metals and Alloys. Pergamon Press.

Ramalingam, B., 1998. Studies of Bonding and Void Nucleation at Inclusion-Matrix Interfaces in Steel. Ph.D. Thesis, Carnegie Mellon University, Pittsburgh, PA, 368 pp.

Rice, J.R. and Tracey, D.M., 1969. Journal of Mechanics and Physics of Solids, 17(1969): 201-217.

Senior, B.A., Noble, F.W. and Eyre, B.L., 1986. Acta Metallurgica, 34(7): 1321-1327.

Winter, M., In: http://www.webelements.com/ (Editor), University of Sheffield. Vol. .

Wojcieszynski, A.J., 1993. Particle spacing and grain size effects on fracture toughness. Ph. D. Thesis, Carnegie Mellon University, Pittsburgh.

7. List of publications and presentations

1. "An Experimental Investigation of Void Nucleation at Manganese Sulfide Inclusions in Austenitic Steel", Bala Ramalingam and W.M. Garrison, Jr. *(in progress)*
2. "Electronic Structure and Bonding in Titanium Carbosulfide", Bala Ramalingam, Jan van Ek, J.M. MacLaren , M.E. McHenry, and W.M. Garrison, Jr. (accepted for publication in Philosophical Magazine B, 1999)
3. "Experimental Investigations of Void Nucleation at Inclusion-Matrix Interfaces in Austenitic Steel", Bala Ramalingam and W.M. Garrison, Jr., *Mini Workshop on Ductile Fracture*, Pennsylvania State University (September 1998)
4. "Studies of Bonding and Void Nucleation at Inclusion-Matrix Interfaces in Steel", Ph. D. Thesis, Carnegie Mellon University (February 1998)
5. "Strength of Inclusion-Matrix Interfaces in Steel"; Bala Ramalingam, J.M. MacLaren, W.M. Garrison, Jr. and M.E. McHenry; 39th Mechanical Working and Steel Processing Conference Proceedings, ISS, Vol. XXXV, pp. 583-595 (1998)
6. "Ab-initio Calculations of Electronic Structure and Properties of Titanium Carbosulfide"; Bala Ramalingam, M.E. McHenry, W.M. Garrison, Jr. and J.M. MacLaren; MRS Symposium Proceedings, Vol. 408, pp. 563-566 (1996)
7. "An Evaluation of an Ultra-High Strength Steel Strengthened by Alloy Carbide and Intermetallic Precipitates", Warren M. Garrison, Jr. and Mark A. Rhoads, Trans. Indian Inst. Met., Vol. 49, No. 3, pp. 151-162 (1996)
8. "Improving the Fracture Toughness of Structural Steels by the Control of Sulfide Type", W.M. Garrison, A.L. Wojcieszynski, B. Ramalingam; High Performance Steels for Structural Applications (International Symposium Proceedings), ASM, pp. 257-268 (1995)
9. "Bulk and Interface Magnetism Involving alpha-MnS and FCC or BCC Iron", Bala Ramalingam, M.E. McHenry, W.M. Garrison, Jr. and J.M. MacLaren; Intermag 95; San Antonio, TX (April 1995)
10. "Alloy Design in Practice", Indian Institute of Metals Lecture, Indian Institute of Technology, Madras, India (February 1995)
11. "Understanding Void Nucleation at Inclusions in Steel", Tata Iron and Steel Company (TISCO), Jamshedpur, India (January 1995)
12. "Understanding Void Nucleation at Inclusions in Steel", Research and Development Center for Iron and Steel, Steel Authority of India Limited, Ranchi, India (January 1995)
13. "Ab-initio Calculations of Electronic Structure and Interfacial Properties of Manganese Sulfide Particles in Steel", Bala Ramalingam, M.E. McHenry, W.M. Garrison, Jr. and J.M. MacLaren; MRS Fall Meeting 1994, Boston, MA

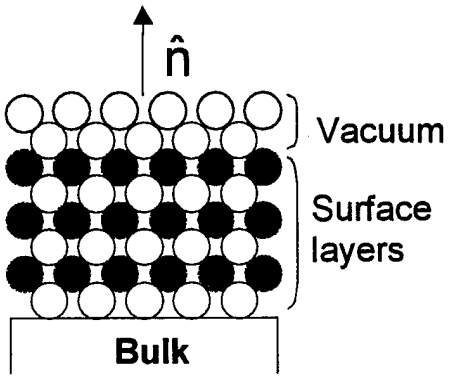

Figure 1: Schematic of a surface calculation setup

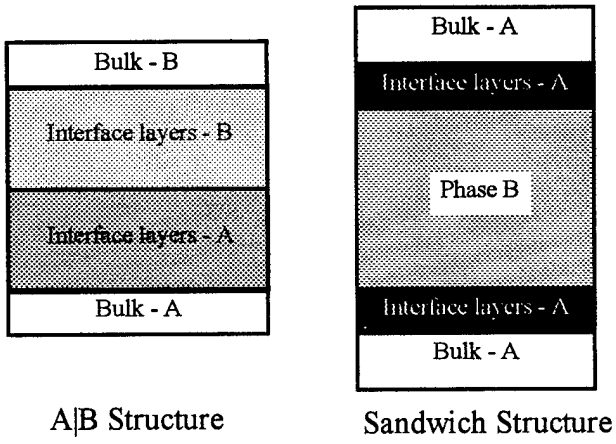

Figure 2: Interface calculation setup – A|B and sandwich structures

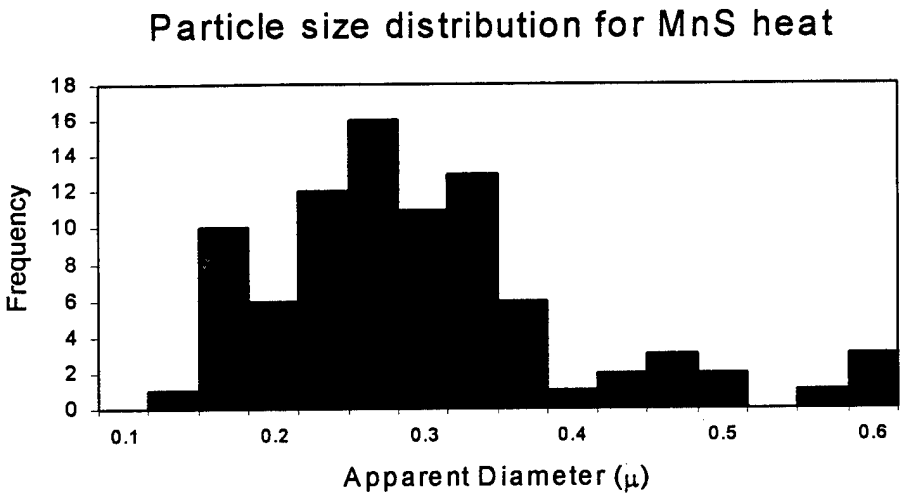

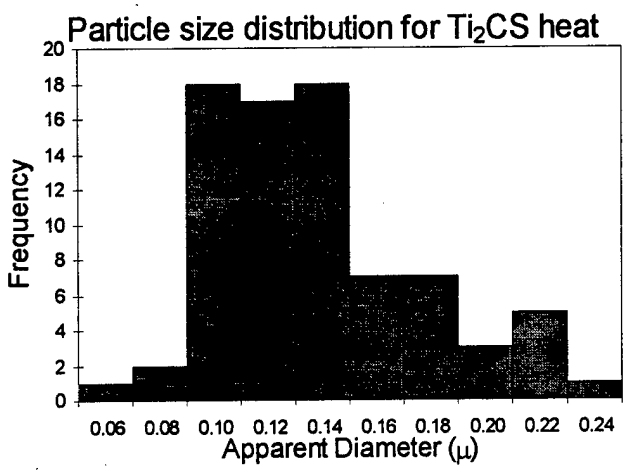

Figure 3: Particle size distribution for the MnS and Ti_2CS heats

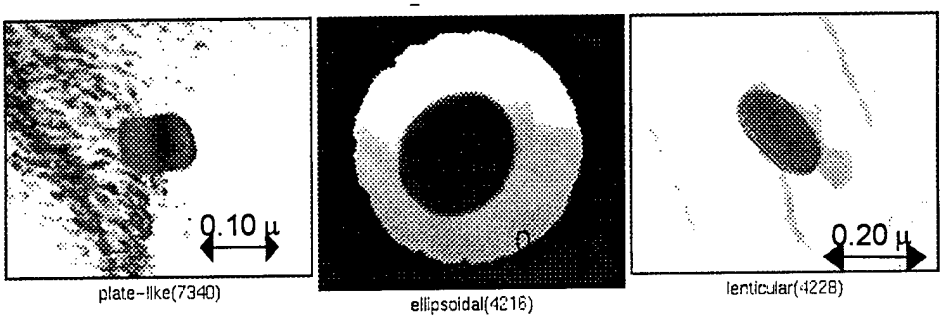

Figure 4: Different particle morphologies of Ti_2CS observed in the TEM

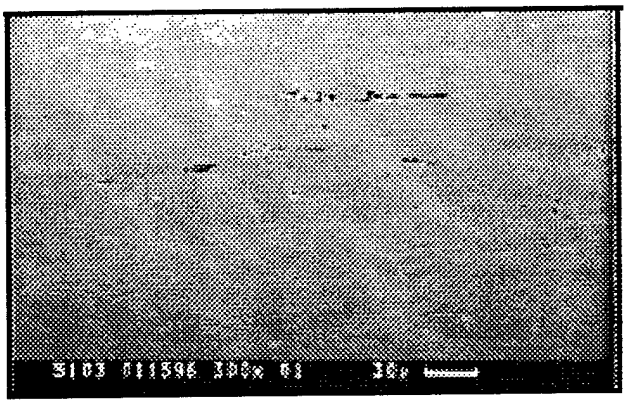

Figure 5: Low magnification SEM image of extended voids in the MnS heat near the fracture surface

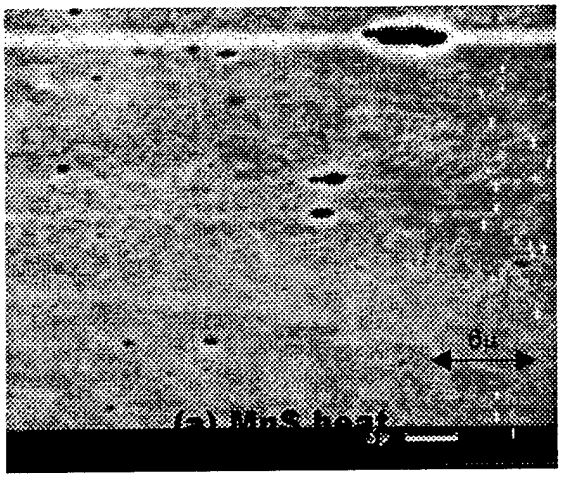

MnS (strain = 0.85)

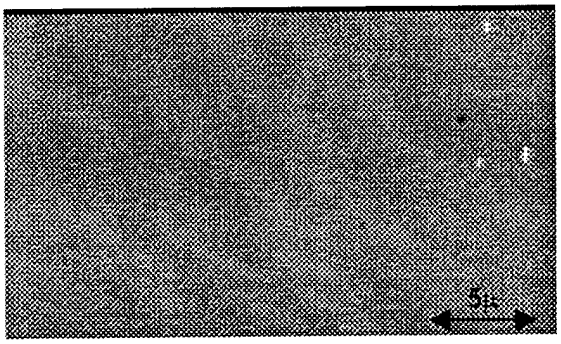

(b) Ti_2CS heat

Figure 6: SEM image of strained specimens (a) MnS specimen at $\varepsilon \sim 0.85$ (b) Ti_2CS specimen at $\varepsilon \sim 1.7$

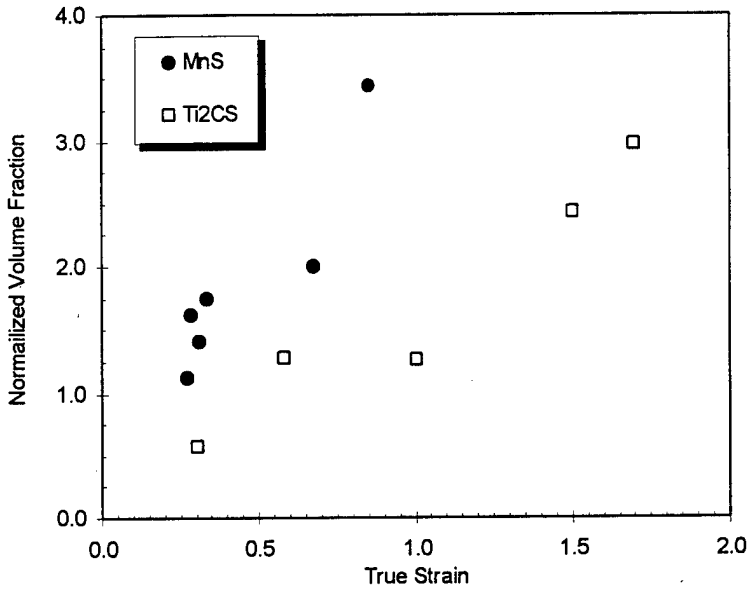

Figure 7: Normalized void volume fraction as a function of true strain for the MnS and the Ti_2CS heats

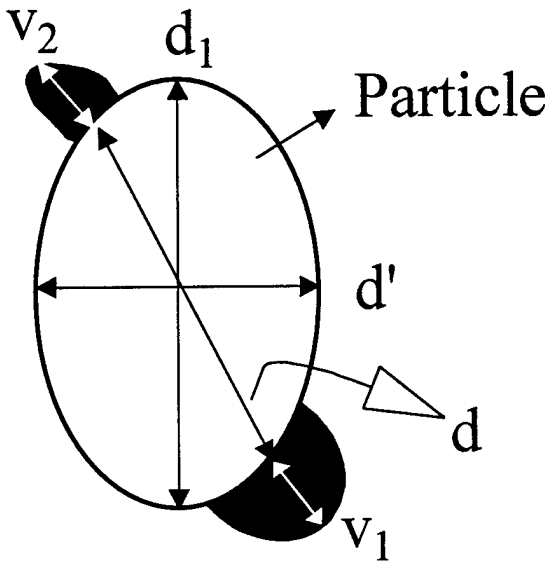

Figure 8: Schematic illustrating the main parameters that were measured for a particle-void combination on a TEM negative

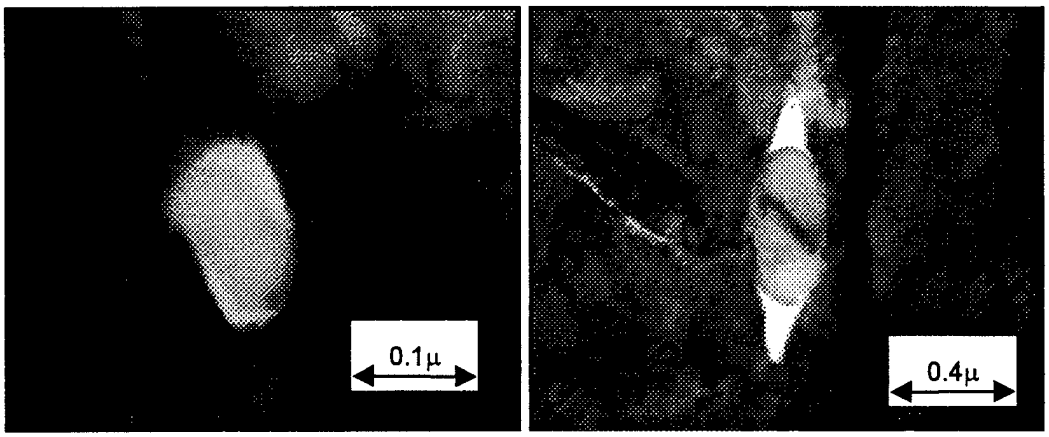

(a) TEM images illustrating voids away from (left), and at (right), particle poles

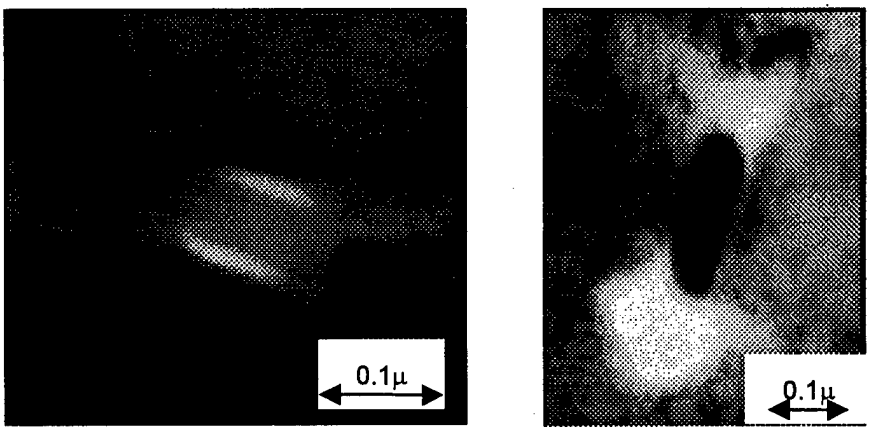

(b) TEM images illustrating voids parallel to (left), and away from (right), particle facets

Figure 9: Orientation of voids with respect to different particle features

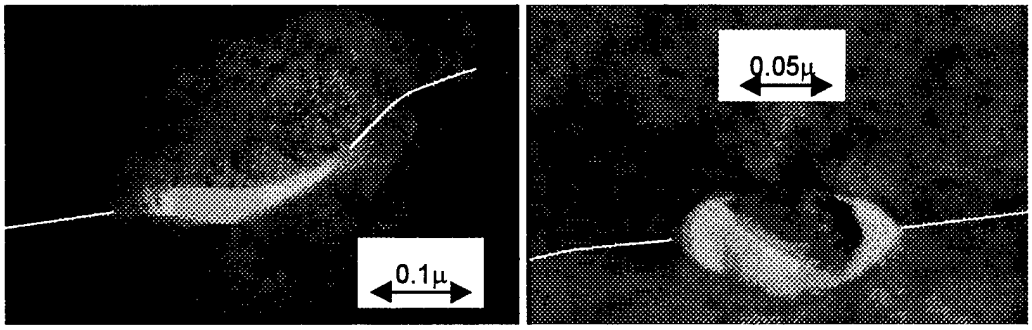

Figure 10: Orientation of voids with respect to grain boundaries (indicated by the white lines)

MnS

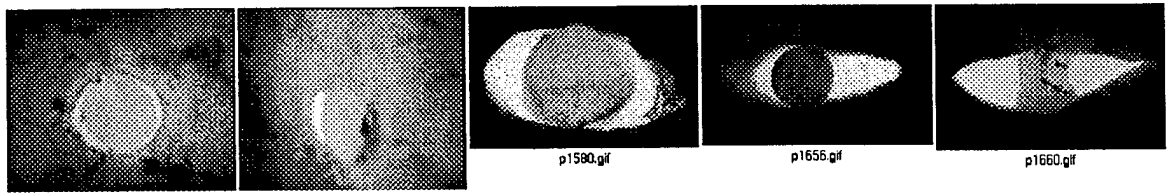

L (μ):	0.143	0.114	0.341	0.250	0.317
VGI:	1.17	1.19	1.54	2.27	4.00

L = longest particle dimension observed

Ti_2CS

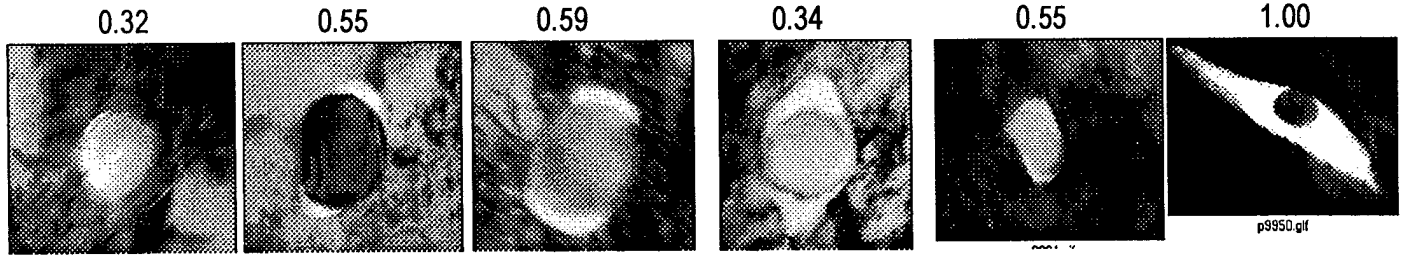

L (μ):	0.156	0.207	0.100	0.095	0.181	0.278
VGI:	1.02	1.22	1.24	1.45	2.00	5.10

Figure 11: Particles in different stages of void nucleation and growth in the two heats. Instead of scale markers, the longest particle dimension has been given for each particle

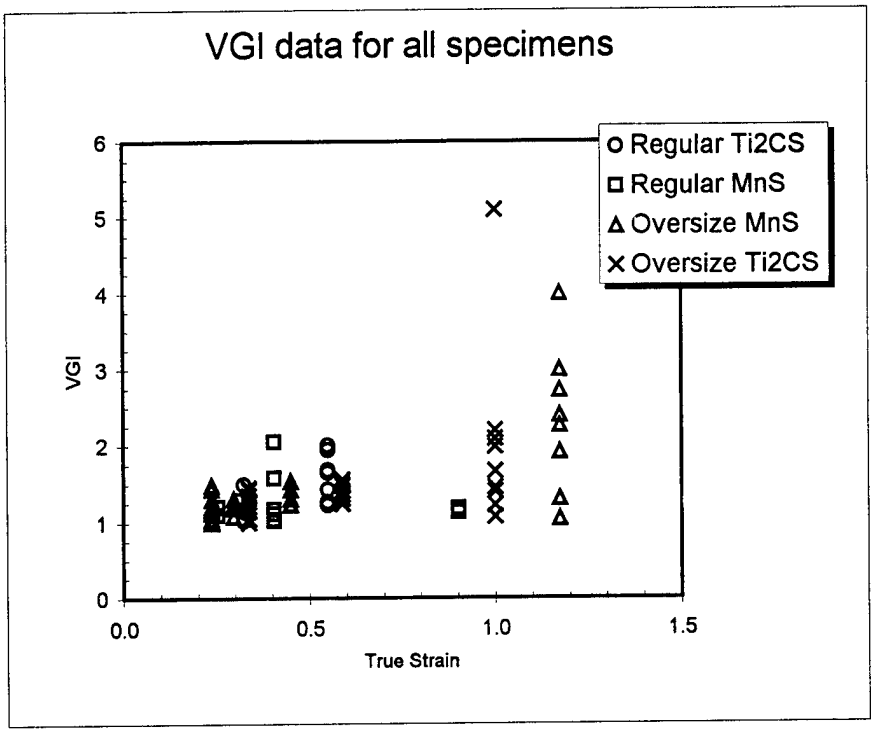

(a)

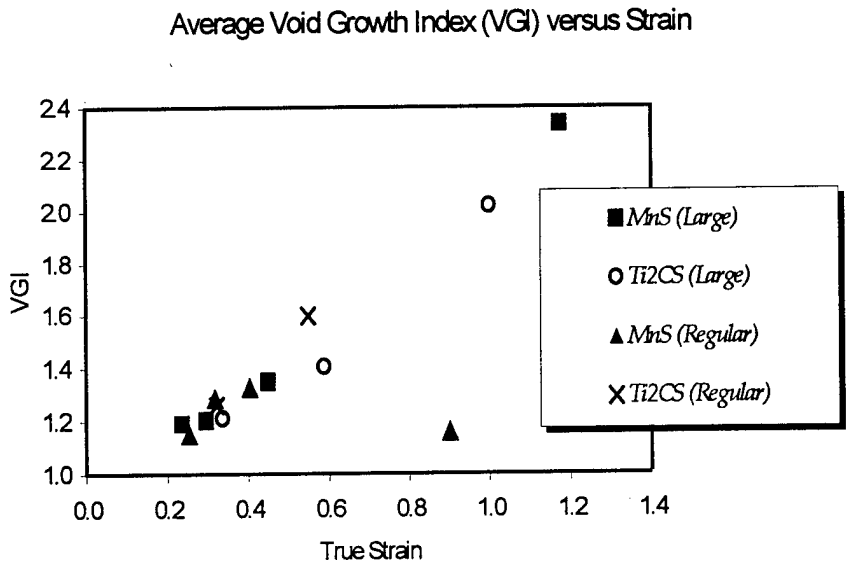

(b)

Figure 12: (a) VGI scattergram showing the observed VGI values as a function of true strain (b) Average VGI versus true strain

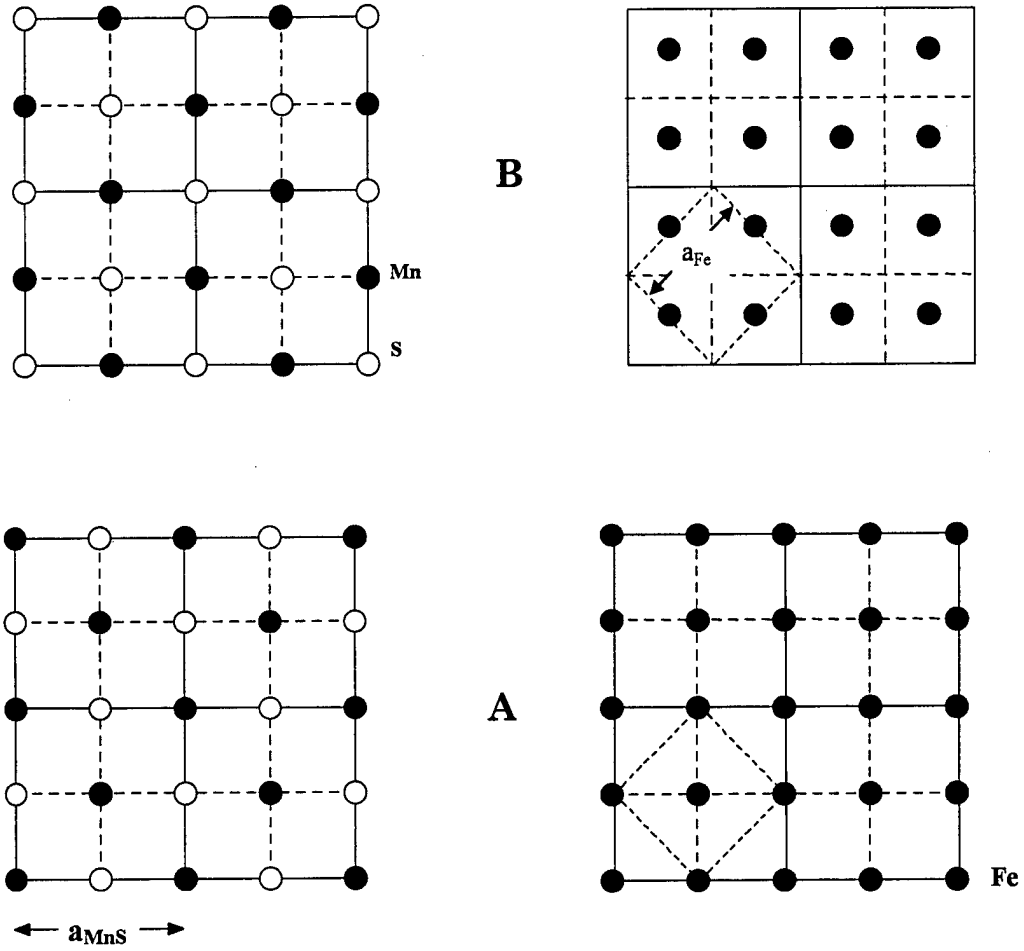

Figure 13: Atomic arrangements in (001) γ-Fe and MnS – the stacking is ABAB...

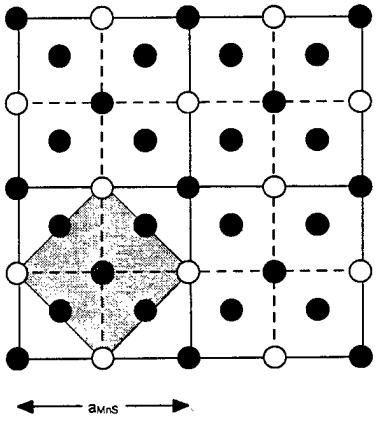

Figure 14: Orientation relationship between γ-Fe and MnS with 2-D unit cell shaded

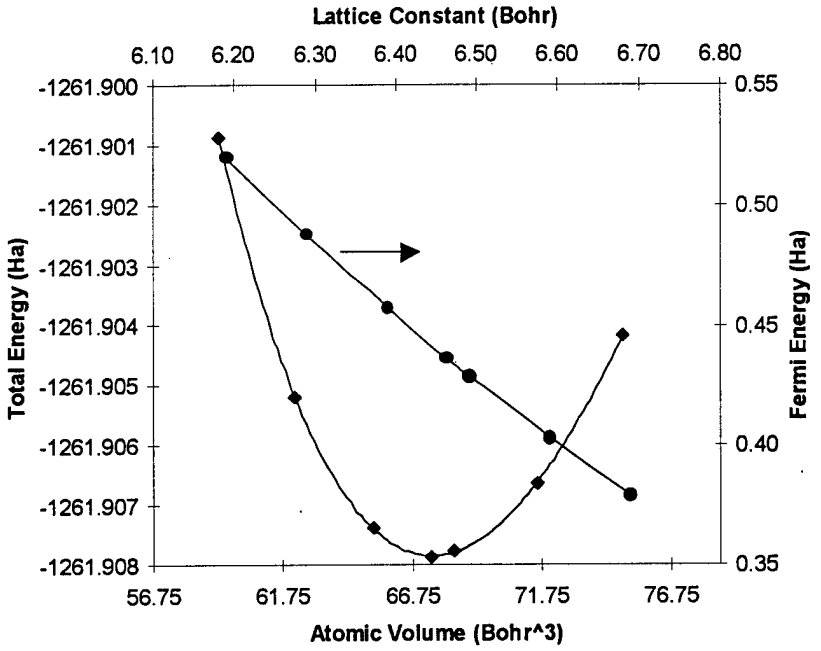

Figure 15: Total energy and Fermi energy as a function of atomic volume for fcc iron

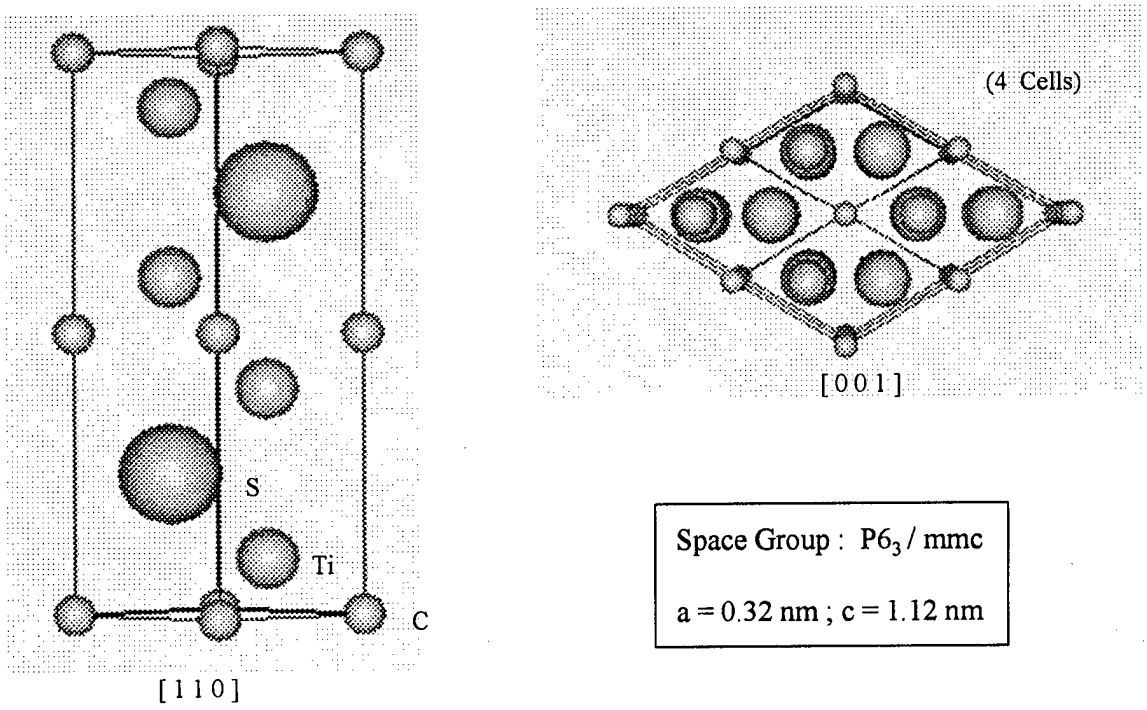

Figure 16: The arrangement of atoms in Ti_2CS as viewed from [110] and [001] crystallographic directions

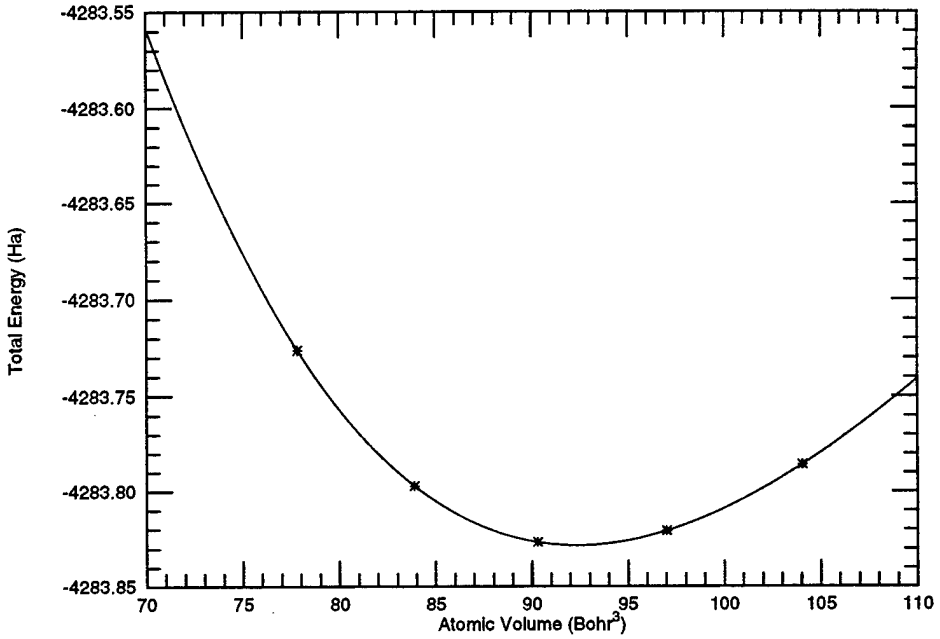

Figure 17: The variation of the total energy per unit cell as a function of the atomic volume in Ti_2CS. The line joining the points is the fourth-order Birch-Murnaghan polynomial (equation 5)

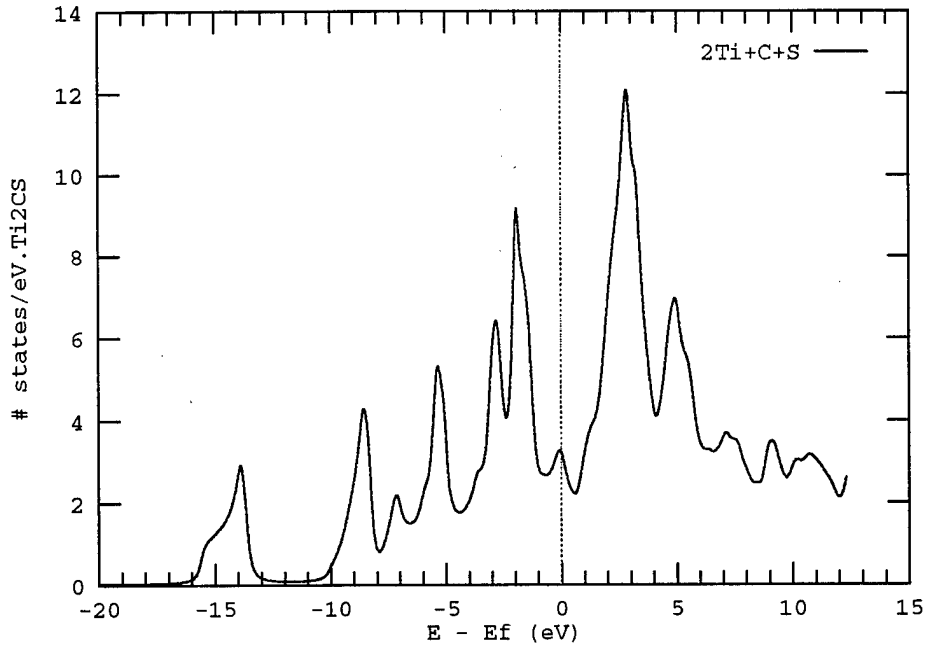

Figure 18: Total (2Ti+C+S) density of states (DOS) in Ti_2CS

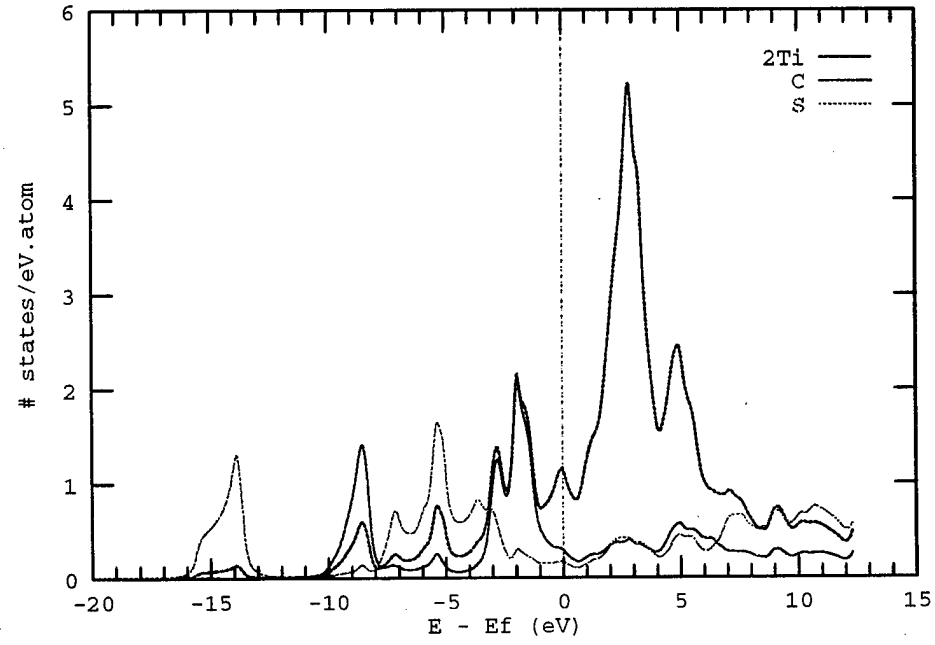

Figure 19: Site-resolved DOS in Ti_2CS

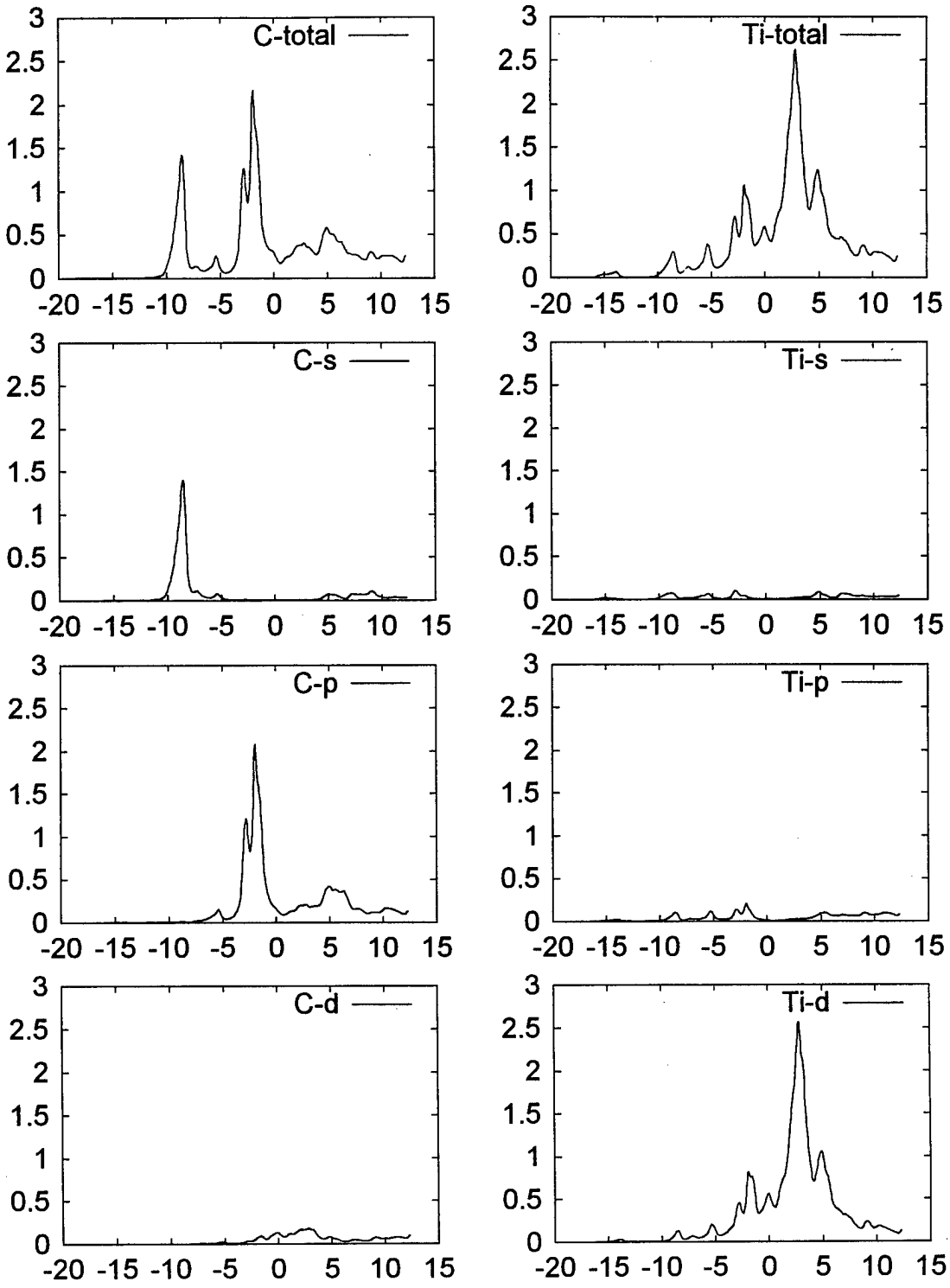

Figure 20: Angular momentum resolved DOS for C and Ti in Ti_2CS {in all curves, the abcissa is the energy in eV relative to the Fermi energy while the ordinate is the number of electronic states per eV.atom}

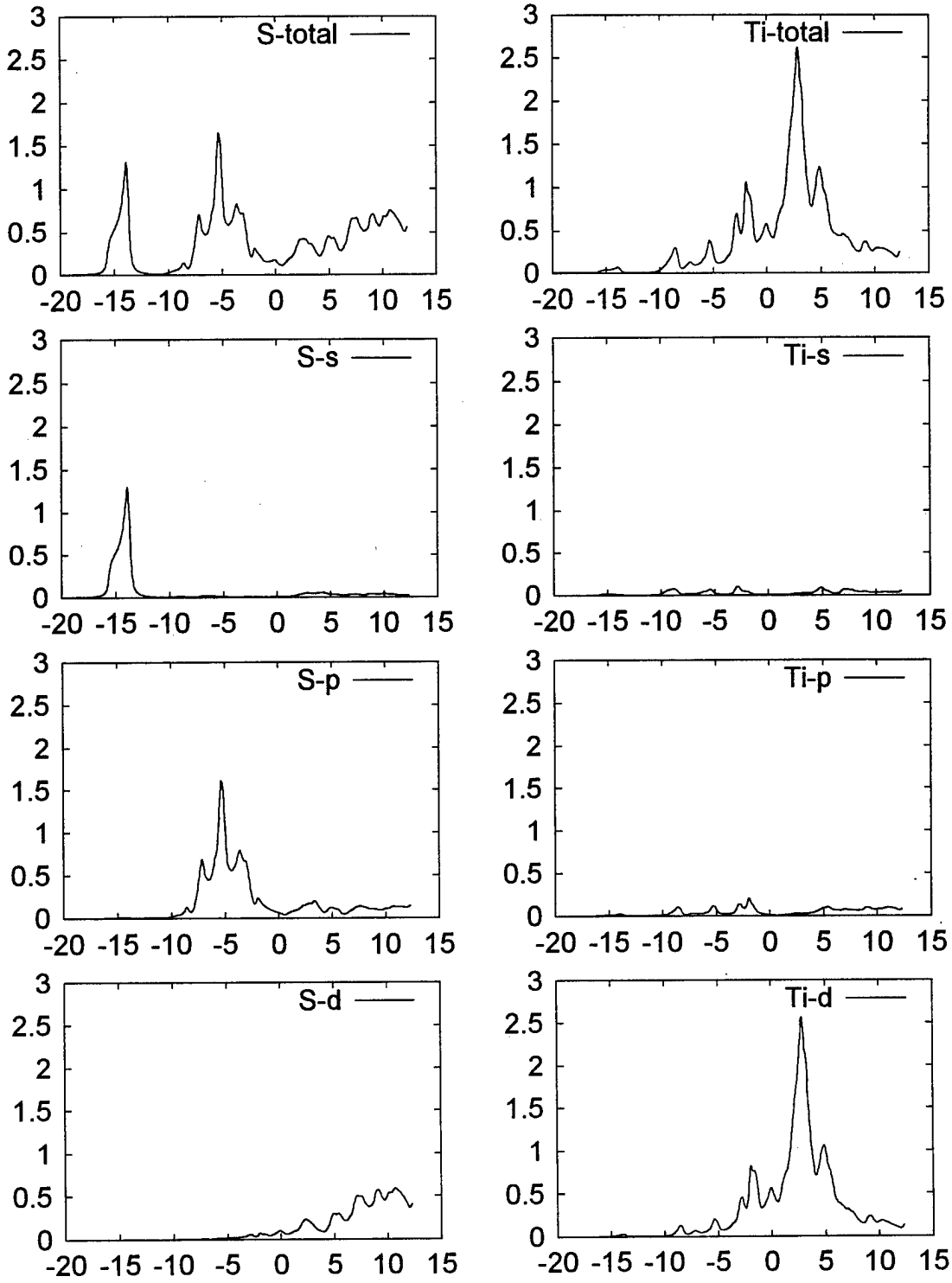

Figure 20: (Continued) Angular momentum resolved DOS in Ti_2CS for S and Ti (see caption in previous page for more details)

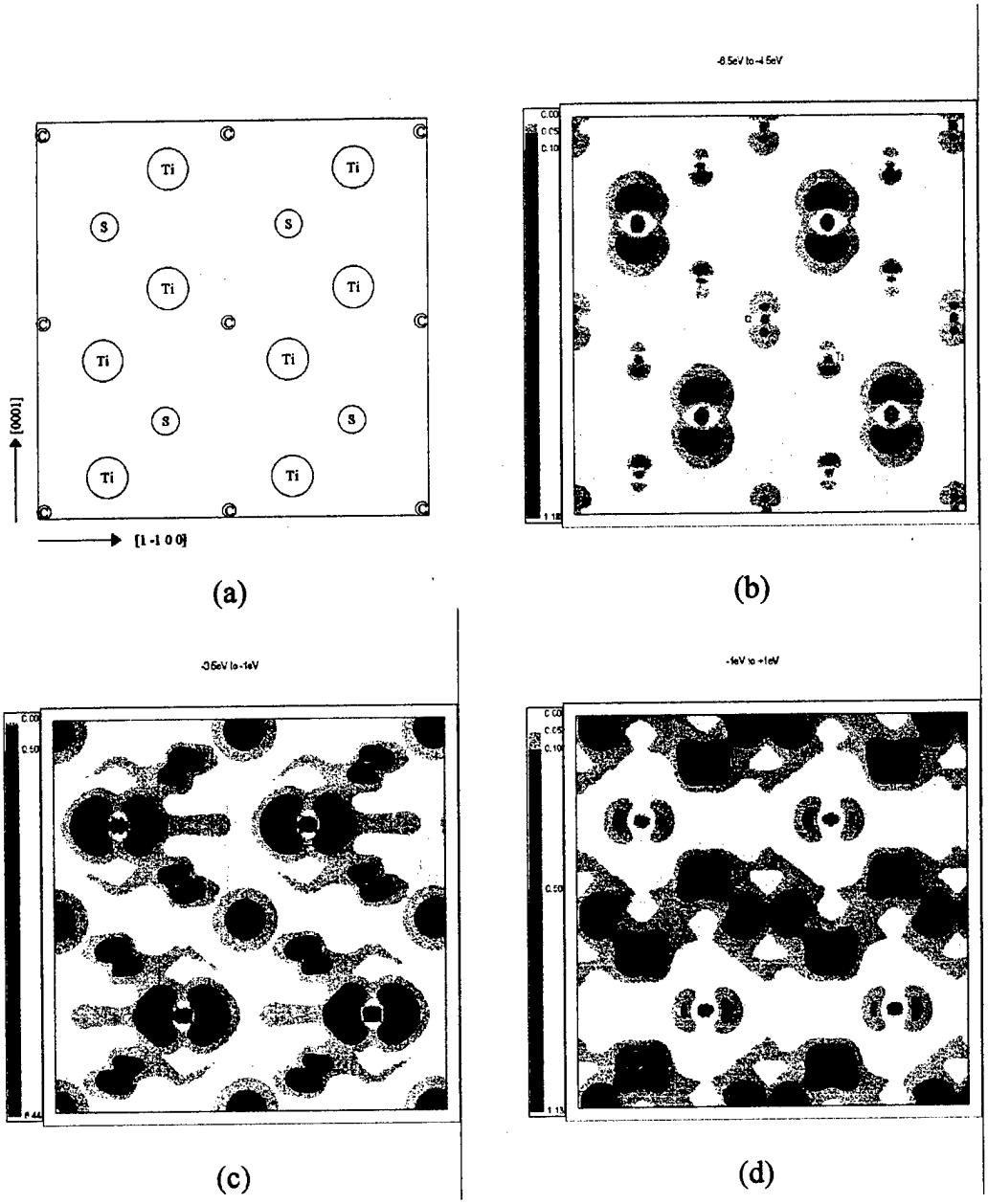

Figure 21

(a) Schematic showing atomic positions in the (1 1 -2 0) plane in Ti_2CS
(b) Charge density contours in the (1 1 -2 0) plane, in the -6.5eV to -4.5eV energy range with respect to the Fermi level. Contours for 0.01, 0.02, 0.05 and 0.10 electrons/Bohr^3 are shown
(c) as for (b), but in the -3.5eV to -1eV energy range with respect to the Fermi level. Contours for 0.03, 0.05, 0.10 and 0.50 electrons/Bohr^3 are shown
(d) as for (c), in the -1eV to +1eV range with respect to the Fermi level. Contour levels as for (c)

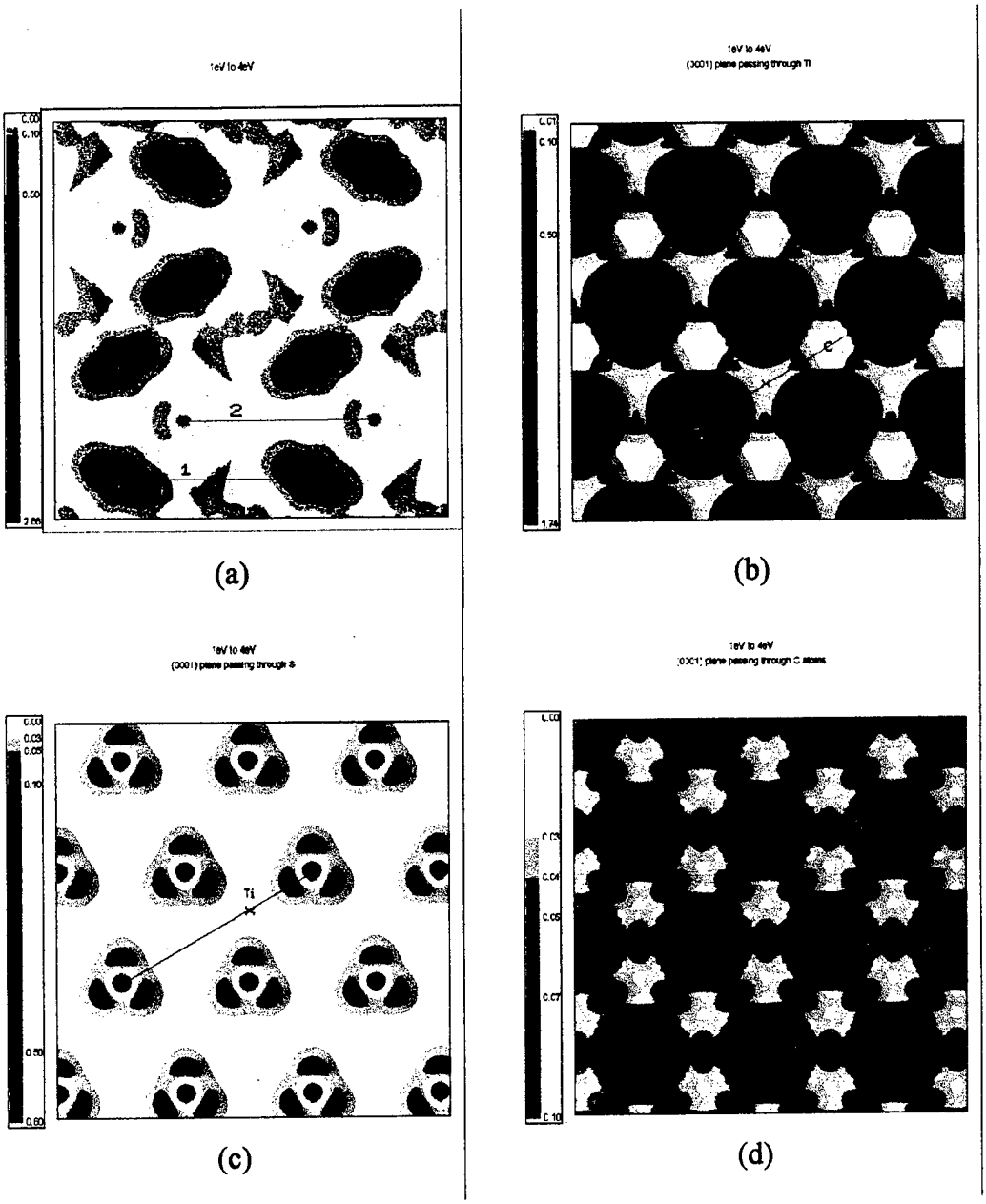

Figure 22

Charge density contours in the +1eV to +eV range with respect to Fermi level:
(a) in the (1 1 -2 0) plane. Contours for 0.03, 0.05, 0.10 and 0.50 electrons/Bohr^3 are shown
(b) in a (0001) type plane passing through titanium atoms. Contours for 0.01, 0.05, 0.10 and 0.50 electrons/Bohr^3 are shown
(c) in a (0001) type plane passing through sulfur atoms. Contours for 0.03, 0.05, 0.10 and 0.50 electrons/Bohr^3 are shown
(d) in a (0001) type plane passing through carbon atoms. Contours for 0.03, 0.04, 0.05, and 0.07 electrons/Bohr^3 are shown

Table 1: Composition of the MnS and Ti_2CS heats of the model austenitic steel

Heat	C	Ni	Cr	Si	Mn	S	P	Ti	N_2^*	O_2^*
G785 (MnS)	.089	38.48	.01	.01	.51	.006	.003	.007	2	12
G786 (Ti_2CS)	.080	39.56	.01	.01	.01	.007	.004	.027	2	10

* N_2 and O_2 in ppm; rest in weight %

Table 2: Summary of tensile properties for specimens after 1100°C austenitizing treatment

	ε_f	R.A. (%)	UTS (MPa)
G785 (MnS)	1.55	78.80	510
G786 (Ti_2CS)	1.96	85.79	516

[a] True fracture strain
[b] Percentage reduction in area
[c] Ultimate tensile strength

Table 3: Inclusion characteristics of the two heats

Heat	Number of particles	f_V	R_o (μ)	X_0 (μ)
G785 (MnS)	89	0.000551	0.202	2.197
G786 (Ti_2CS)	79	0.000301	0.095	1.262

f_V – Volume fraction; R_o – Average particle radius; X_o – Average 3-D near-neighbor spacing

Table 4:k-point and plane-wave convergence of γ-Fe bulk (001) calculations

	Number of k-points sampled in the irreducible Brillouin zone wedge		
	10	36	136
Lattice constant (Bohrs)	6.48	6.46	6.46
Bulk Modulus (Mbar)	3.08	3.25	3.22

	Number of interstitial plane wave rings used[a]		
	6	8	10
Total energy (Ha)	-2542.01334	-2542.02035	-2542.02092
Fermi energy (Ha)	0.43889	0.43864	0.43862

[a] at a lattice constant of 6.46 Bohrs using 36 k-points

Table 5: Layer convergence of the surface energy in MnS

Number of vacuum layers	Number of MnS surface layers	Surface energy (J/m^2)
2	4	2.09
2	5	2.02
3	5	2.02
2	6	2.10

Table 6: Layer convergence of the γ-Fe/MnS interfacial energy

Number of Fe layers (each side)	Number of MnS layers	Interface energy (J/m^2)
3	7	1.41
3	9	1.40
4	7	1.42
4	9	1.41

Table 7: Elemental bond length, and the covalent and ionic radii of the constituent atoms of Ti_2CS

Element	Covalent		Elemental Bond Length		Ionic	
	Angs.	Bohr	Angs.	Bohr	Angs.	Bohr
Carbon	**0.77**	**1.455**	1.426	2.695	--	--
Sulfur	1.02	1.928	2.050	3.874	**1.84**	**3.477**
Titanium	**1.36**	**2.570**	2.896	5.473	**0.68**	**1.285**

Table 8: Summary of computational results for all bulk and surface systems considered in the present work (compared with experimental results if available)

	Material	Lattice Constant (a.u.)		Bulk Modulus (Mbar)		Magnetic Moment (μ_B)	
		Current Results	Experimental[b]	Current Results	Experimental	Current Results	Experimental
BULK	Fe (fcc)	6.46	6.78	3.25		0.00	0.00
	Fe (bcc)[a]	5.29	5.41	2.16	1.68—1.73	2.16	2.12
	MnS	8.70	9.81	0.96-1.06[e]		2.94 Mn ; 0.11 S	
	Ti_2CS	6.26	6.07[c]	2.47	No data available	---	---
	TiC[f]	8.13	8.18[d]	4.73	2.88[f]	---	---
	ZrC	8.96	8.86	4.89	2.65[f]	---	---

[a] experimental values taken from Table II of Hathaway et. al. (1985), Phys. Rev. B, 31(12), 7603-11.
[b] experimental lattice constants from Pearson (unless otherwise mentioned) extrapolated to 0 K using approximate coefficients of thermal expansion; value for ZrC not temperature compensated
[c] value not extrapolated to 0 K because coefficient of thermal expansion is not known
[d] value taken from Neckel et al. (1976), J. Phys. C: Solid State Phys., 9, 579-92.
[e] 3rd and 4th order polynomials gave 0.96 Mbar while 5th and 6th order polynomials yielded 1.06 Mbar
[f] Data from Table 2.1 of "Electronic structure of refractory carbides and nitrides", Gubanov et al., Cambridge University Press, 1994.

		Surface energy (J/m^2)	Work function (eV)
SURFACE	γ-Fe	2.57	6.43
	MnS	2.09	4.95
	TiC[a]	1.83	5.47
	ZrC	1.79	5.03

[a] Lattice constant of 8.10 Bohr used for TiC and a = 9.14 Bohr used for all other systems